The Planetary Science Journal, 3:210 (21pp), 2022 September https://doi.org/10.3847/PSJ/ac880d

Anticipated Geological Assessment of the (65803) Didymos–Dimorphos System, Target of the DART–LICIACube Mission

M. Pajola[1], O. S. Barnouin[2], A. Lucchetti[1], M. Hirabayashi[3], R.-L. Ballouz[2], E. Asphaug[4], C. M. Ernst[2], V. Della Corte[5], T. Farnham[6], G. Poggiali[7,8], J. M. Sunshine[6], E. Mazzotta Epifani[9], N. Murdoch[10], S. Ieva[9], S. R. Schwartz[11], S. Ivanovski[12], J. M. Trigo-Rodriguez[13], A. Rossi[14], N. L. Chabot[2], A. Zinzi[15,16], A. Rivkin[2], J. R. Brucato[7], P. Michel[17], G. Cremonese[1], E. Dotto[9], M. Amoroso[15], I. Bertini[18], A. Capannolo[19], A. Cheng[2], B. Cotugno[20], M. Dall'Ora[21], R. T. Daly[2], V. Di Tana[20], J. D. P. Deshapriya[9], I. Gai[22,23], P. H. A. Hasselmann[9], G. Impresario[15], M. Lavagna[19], A. Meneghin[7], F. Miglioretti[20], D. Modenini[22,23], P. Palumbo[18], D. Perna[9], S. Pirrotta[15], E. Simioni[1], S. Simonetti[20], P. Tortora[22,23], M. Zannoni[22,23], and G. Zanotti[19]

[1] INAF-Osservatorio Astronomico di Padova, Padova, Italy; maurizio.pajola@inaf.it
[2] Johns Hopkins University Applied Physics Laboratory, MD, USA
[3] Auburn University, AL, USA
[4] University of Arizona, AZ, USA
[5] INAF-Istituto di Astrofisica e Planetologia Spaziali, Roma, Italy
[6] University of Maryland, Department of Astronomy, MD, USA
[7] INAF-Osservatorio Astrofisico di Arcetri, Firenze, Italy
[8] LESIA-Observatorie de Paris PSL, France
[9] INAF-Osservatorio Astronomico di Roma, Monte Porzio Catone, Roma, Italy
[10] Institut Supérieur de l'Aéronautique et de l'Espace (ISAE-SUPAERO), Université de Toulouse, France
[11] Planetary Science Institute, University of Arizona, AZ, USA
[12] INAF-Osservatorio Astronomico di Trieste, Trieste, Italy
[13] Institute of Space Sciences (ICE, CSIC) and Institut d'Estudis Espacials de Catalunya (IEEC), Spain
[14] IFAC-CNR, Sesto Fiorentino, Firenze, Italy
[15] Agenzia Spaziale Italiana, Roma, Italy
[16] Space Science Data Center—ASI, Roma, Italy
[17] Université Côte d'Azur, Observatoire de la Côte d'Azur, CNRS, Laboratoire Lagrange, Nice, France
[18] Università degli Studi di Napoli "Parthenope", Dipartimento di Scienze & Tecnologie, Centro Direzionale, Napoli, Italy
[19] Politecnico di Milano—Bovisa Campus, Dipartimento di Scienze e Tecnologie Aerospaziali, Milano, Italy
[20] Argotec, Torino, Italy
[21] INAF-Osservatorio Astronomico di Capodimonte, Napoli, Italy
[22] Alma Mater Studiorum—Università di Bologna, Dipartimento di Ingegneria Industriale, Forlì, Italy
[23] Alma Mater Studiorum—Università di Bologna, Centro Interdipartimentale di Ricerca Industriale Aerospaziale, Forlì, Italy
Received 2022 February 8; revised 2022 August 1; accepted 2022 August 1; published 2022 September 14

Abstract

On 2022 September 26, the DART spacecraft will impact the surface of Dimorphos, the ∼160 m size satellite of the binary near-Earth asteroid (NEA) (65803) Didymos. What will be observed on the surfaces of both asteroids and at the DART impact site is largely unknown, beyond the details of Didymos revealed by previous Arecibo and Goldstone radar observations. We present here the expected DART and LICIACube observations of the Didymos system and discuss the planned mapping strategies. By searching similar geological features and processes identified on other NEAs, we constrain the impact conditions that DART might encounter at Dimorphos, assessing both the asteroid's surface and interior structure.

Unified Astronomy Thesaurus concepts: Asteroids (72); Asteroid surfaces (2209); Asteroid satellites (2207)

1. Introduction

The NASA Double Asteroid Redirection Test (DART; Rivkin et al. 2021) mission is the first to test a full-scale planetary defense technology, namely the kinetic impact method,[24] using for target the moon of the binary near-Earth asteroid (NEA) (65803) Didymos (Cheng et al. 2018). Radar observations indicate that the primary member, Didymos is a top-shaped object with a diameter of 780 m and a conspicuous equatorial bulge (Naidu et al. 2020). The secondary moonlet, Dimorphos, is characterized by a maximum diameter of ∼163 m whose shape is not well known. The latter orbits at a distance of ∼1.1 km with a period of 11.9216289 ± 0.0000028 hr. A complete description of the physical and dynamical parameters of the system can be found in Fang & Margot (2012a), Michel et al. (2016), Cheng et al. (2016), Naidu et al. (2020), Pravec et al. (2006), Pravec et al. (2012), Pravec et al. (2016), and Pravec et al. (2022). After launch on 2021 November 23, at 10:21 p.m. PST (2021 November 24, 6:21 a.m. UTC), the DART spacecraft (impact mass of about 650 kg) will impact Dimorphos on 2022 September 26 (at 7:14 p.m. EDT, at 11:14 p.m. UTC), at around 6.15 km s^{-1}, in order to modify its orbit around the primary member of the system. The expected change in the secondary orbital period is about 10 minutes, which will be measured by ground-based telescopes

[24] The first planetary-scale impact experiment on a small body was the NASA/Deep Impact mission to comet 9P/Tempel 1. More details on its key results relevant to the DART/LICIACube mission are presented in the Appendix.

in the months following the DART impact (Cheng et al. 2018; Rivkin et al. 2021).

In order to provide the best possible pre-impact surface assessment of Dimorphos, the spacecraft carries the Didymos Reconnaissance and Asteroid Camera for Optical navigation (DRACO) (Fletcher et al. 2018). This instrument, derived from the LOng-Range Reconnaissance Imager (LORRI) on New Horizons (Cheng et al. 2008), is a high-resolution panchromatic (400–1000 nm) catadioptric Ritchey–Chrétien telescope, with an instantaneous field of view (IFOV) of 5 μrad (binned pixels), a 208 mm aperture, $f/12.6$, and a 0.°29 field of view (Fletcher et al. 2018). Just prior to impact, DRACO will image Dimorphos at <0.5 m pixel^{-1}. Piggy-backing on the DART spacecraft during the launch, the Italian Space Agency (ASI) Light Italian Cubesat for Imaging of Asteroids (LICIACube; Dotto et al. 2021) will travel together with DART to the target. Released 15 days before impact, the LICIACube spacecraft will observe the binary asteroid and the DART impact from a close approach (CA) distance of ∼51 km. Two optical imagers provide the observations: the LICIACube Explorer Imaging for Asteroid (LEIA), which is a 2048 × 2048 pixel high-resolution panchromatic camera with an IFOV of 25 μrad, and the LICIACube Unit Key Explorer (LUKE), which is a 2048 × 1048 pixels wide-angle three-band color imager (RGB Bayer pattern filter) with an IFOV of 78 μrad (Dotto et al. 2021). At CA, it will be possible to image Dimorphos' surface with a spatial scale of <2 m pixel^{-1}, complementing the DRACO observations performed during the pre-impact phase. Images acquired by LICIACube immediately after the impact will contribute to the determination of the momentum transfer caused by the DART impact by means of the characterization of the structure and evolution of the ejecta plume. LICIACube will also allow a multiresolution geological characterization of ∼2/3 of the illuminated surface area of both Dimorphos and Didymos.

Both DRACO cameras and LEIA and LUKE will provide substantial geological information on the Didymos system before the arrival of the ESA Hera spacecraft (Michel et al. 2022), which will characterize in detail the post-impact geology of the system. Hera will launch in 2024 to rendezvous with Didymos in 2026 and fully characterize the asteroid system, including the mass and volume of Dimorphos and the outcome of the DART impact (crater size and morphology). Hera will explore the geology and composition of Dimorphos and Didymos using a broad suite of instruments and two cube satellites (see Michel et al. 2022 for details).

Here, we review the latest planned DRACO and LICIACube observations and discuss what we will be able to determine about the geological properties of the Didymos–Dimorphos system and the DART impact site. This work represents an update of the geologic investigations in Cheng et al. (2018) by including a discussion of LICIACube imaging. Furthermore, we leverage spacecraft observations of other NEAs as a means to assess the geological properties we will be able to determine at Didymos, especially in light of recent results from the OSIRIS-REx and Hayabusa2 mission. We focus in particular on those factors that play a key role in the outcome of the DART impact and its ability to deflect Dimorphos, including those that may influence measures of the momentum transfer efficiency (β; Rivkin et al. 2021). We will also consider what can be more broadly learned about the origin of Dimorphos and the overall Didymos system.

2. Expected DART/DRACO and LICIACube/LEIA–LUKE Imaging Data Sets and Products

The DRACO, LEIA, and LUKE data sets will comprise complementary images acquired at different viewing geometries and phase angles. DRACO will acquire the highest-spatial-resolution images of both Didymos and Dimorphos, including the most detailed picture of the DART impact site, but DRACO images are limited to one approach view of the asteroids. LEIA and LUKE will acquire images both before and after the impact from several viewing geometries as it flies by the system, thereby evaluating the outcome of the impact and its effects on the Dimorphos' surface, and characterizing areas of the asteroids unseen by DRACO.

We here summarize the image acquisitions from DRACO, LEIA, and LUKE that will be used in the geological assessment of the Didymos–Dimorphos system. In DRACO's case, a detailed description of the observations planned throughout the mission is presented in Rivkin et al. (2021). A complete description of LEIA's and LUKE's planned imaging campaign before, during, and after the DART impact is presented in Dotto et al. (2021).

2.1. DRACO Planned Observations

Beginning ∼4 hr before impact, DRACO images will be acquired and immediately downlinked approximately every second. During the bulk of this time, Didymos and Dimorphos will appear as small points of light in each image. Even an hour before impact, when the DART spacecraft will shift to targeting Dimorphos, Didymos will only span 6–7 pixels and Dimorphos 1–2 pixels. It is the final few minutes of DRACO images that will be useful for characterizing the shapes, characteristics, and geology of the asteroids, and the final few seconds of images will be useful for characterizing the impact site at the scale of the spacecraft. During this entire terminal phase, the DRACO imaging data set will be characterized by a phase angle of ∼60°, hence providing good acquisitions to detect surface features such as craters and boulders. In particular, as an example of what the DRACO camera will get (Figure 1):

1. 200 s before the impact (*T0*), the downlinked image contains all of Didymos, with an expected spatial scale of 6 m pixel^{-1};
2. 120 s before *T0*, the downlinked DRACO image contains part of Didymos and will be taken at a spatial scale of 3.5 m pixel^{-1};
3. 20 s before *T0*, DRACO achieves its requirement to image Dimorphos at a scale of 0.66 m pixel^{-1};
4. 16 s before *T0*, DRACO will image all of Dimorphos at a spatial scale of 0.5 m pixel^{-1};
5. Higher-resolution images will continue to be acquired in the final seconds of the DART spacecraft operations, which end upon impact. Planned real-time Deep Space Network (DSN) coverage enables the downlink of these images to Earth, including images acquired until the final 2–5 s before *T0* (down to spatial scale ∼6–15 cm pixel^{-1}).

2.2. LEIA and LUKE Planned Observations

The LICIACube spacecraft will acquire images of the Didymos system with both LUKE and LEIA cameras. In order to observe the ejecta cone and possibly the target surface if not obscured by ejecta, the current imaging baseline (Dotto et al. 2021) is to collect three images at the maximum frame rate possible and with differing integration times.

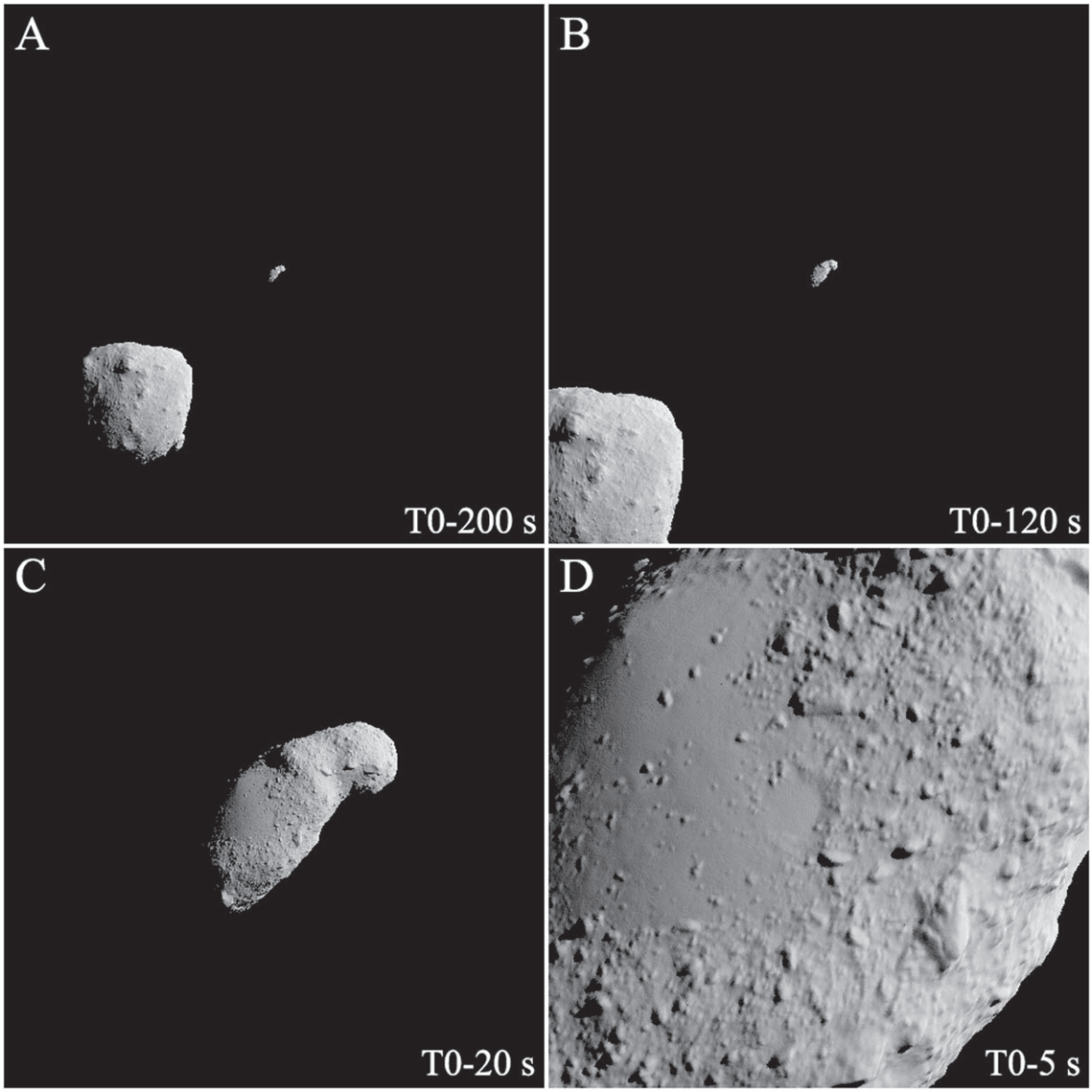

Figure 1. The DRACO simulated images obtained at 200 s (A), 120 s (B), 20 s (C), and 5 s (D) before DART impact. For all panels, Didymos is represented by the scaled shape model of Ryugu, while Dimorphos is the scaled version of Itokawa. Images are 512 × 512 pixel windows like those that will be streamed directly to Earth in real time.

LICIACube will observe the DART impact from a safe distance of ∼1250 km, with a LEIA spatial scale of ∼31 m at *T0* and a phase angle of 58°, Figure 2. The CA to Dimorphos will be then reached ∼165 s after *T0*, at a distance of 51 km and a maximum spatial scale of 1.38 m pixel^{-1} (Figure 3). The minimum phase angle achieved will be ∼43°, but this value will rapidly change to 90° in less than 15 s, already reaching 110° 30 s after CA (Figure 2). In this timeframe, LEIA collects multiple images of the nonimpacted hemisphere of Dimorphos (Figure 3) with spatial scales ranging from a few meters to decameters. This data set will also return images of the illuminated areas of Didymos not observed by DRACO.

Like LEIA, LUKE images the illuminated portions and nonimpacted sides of Dimorphos and Didymos (Dotto et al. 2021). This camera will capture color RGB data in the visible (Poggiali et al. 2022). The color information will be at a spatial scale of <10 m pixel^{-1} (maximum will be ∼4.8 m pix^{-1} at CA) and follows the same range of phase angles as LEIA, changing rapidly within a few tens of seconds.

3. Insights on Didymos–Dimorphos Surface Geology from Prior NEA Encounters and Numerical Models

Insights on what the geological conditions at impact might be when DART strikes Dimorphos can be obtained from past spacecraft encounters with other NEAs. Among all visited asteroids, five NEAs (Figure 4) have been observed at close range: (433) Eros (Veverka et al. 2000), (25143) Itokawa (Fujiwara et al. 2006), (4179) Toutatis (Huang et al. 2013), (162173) Ryugu (Watanabe et al. 2019), and (101955) Bennu (Lauretta et al. 2019a).

Observations of these bodies led to new views on the geological nature of asteroids (see reviews by Murdoch et al. 2015 and Walsh 2018 and references therein; see also the Appendix). Indeed, the wealth of high-resolution data taken on

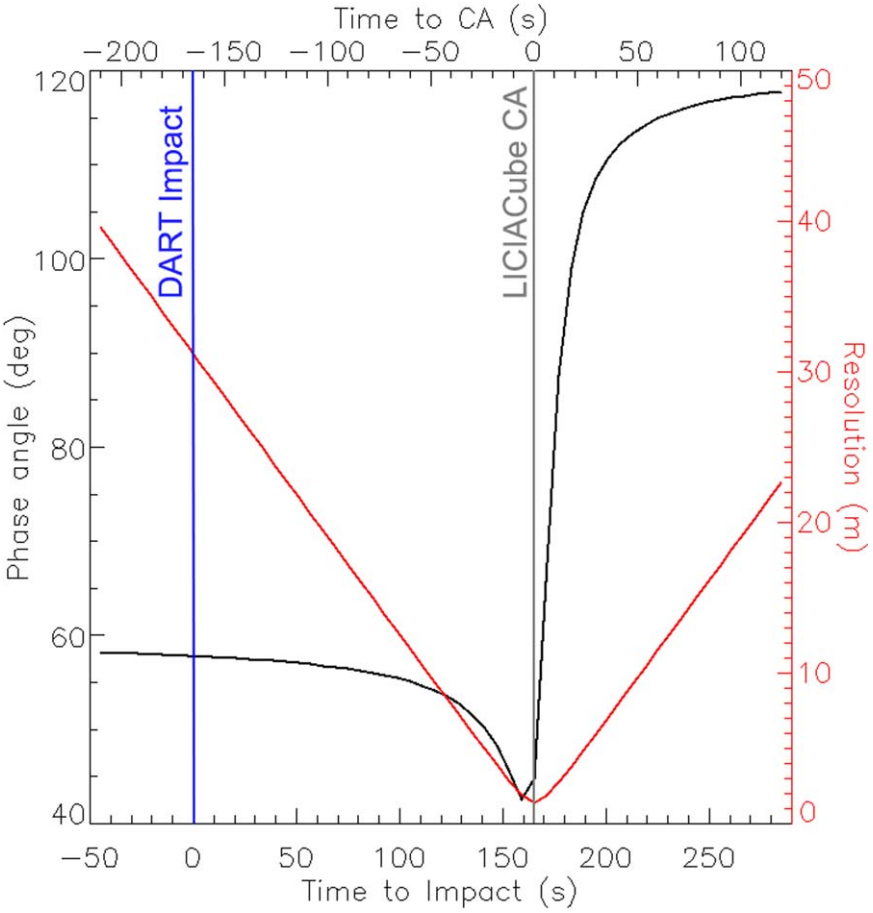

Figure 2. Phase angles and resolutions of the LEIA acquisitions that will be taken from *T0* − 50 s to *T0* + 290 s. The red curve shows resolution as a function of time. The black curve shows phase angle as a function of time.

these objects reveals that their complex surfaces result from an interplay between the geochemical and structural properties of an asteroid (Murdoch et al. 2015) inherited from a parent body and the subsequent geological processes including catastrophic disruption and reaccumulation (Michel et al. 2001; Nakamura et al. 2008; Barnouin et al. 2019; Michel et al. 2020; Tatsumi et al. 2021). This interplay controls the properties of the asteroid's interior and shape, which, with their surface properties and composition,[25] influences any attempt to deflect an asteroid in a planetary defense scenario to protect Earth (Tanbakouei et al. 2019). Therefore, assessing the geology of an NEA provides clues to how it has evolved, what its internal structure may look like, and how it might respond to any attempted deflection (e.g., Gehrels 1994; Perna et al. 2013). In particular, knowledge of the geological nature of Dimorphos' surface, i.e., whether it is smooth or boulder rich (Durda et al. 2011; Guettler et al. 2012; Tatsumi & Sugita 2018; Walsh et al. 2019; Jawin et al. 2022), whether its surface has steep slopes (Barnouin et al. 2019), or whether the surface shows signs of being unusually weak or strong (Arakawa et al. 2020; Lauretta et al. 2022; Barnouin et al. 2022; Walsh et al. 2022) is especially critical for the DART impactor to understand how momentum is transferred, hence influencing the efficacy of deflection (Cheng et al. 2018).

3.1. Rubble Piles and Binary Asteroids: Didymos–Dimorphos Case Study

Besides spacecraft observations, the coupling of collisional physics' numerical models (e.g., Melosh & Ryan 1997; Benz & Asphaug 1999) and the analyses of asteroids' shapes and spins (Harris et al. 2009) have suggested that the vast majority of asteroids between ∼0.2 and 10 km in size are rubble piles, i.e., they are nonmonolithic bodies that consist of numerous pieces of rocks that coalesced under the influence of gravity. This means that small asteroids have therefore very different surface and interior geophysics from large asteroids like, e.g., (4) Vesta (reviews by Asphaug et al. 2002; Walsh 2018) or (21) Lutetia (Sierks et al. 2011), which were never globally disrupted and are subject to much greater gravitational compaction. Consistent with these model expectations, sub-kilometer asteroids Itokawa (0.3 km), Bennu (0.5 km), and Ryugu (0.9 km) do appear to be rubble piles (e.g., Fujiwara et al. 2006; Barnouin et al. 2019; Watanabe et al. 2019). The first evidence for this is

[25] From a taxonomical-compositional perspective (Tholen 1989; Tholen & Barucci 1989) Eros, Itokawa, and Toutatis belong to the same S-type class as Didymos and Dimorphos (Eros being the largest, while Dimorphos being the smallest). S-type asteroids possess evolved compositions, with siliceous mineralogy characterized by a mixture of olivine, pyroxene, and Fe–Ni metal (Bus & Binzel 2002a, 2002b). These asteroids are probably the source of ordinary chondrites (e.g., McCoy et al. 2001; Tsuchiyama et al. 2011). The latter two NEAs possess pristine carbonaceous compositions that are dark. Ryugu is a C-type asteroid while Bennu is a B type. The main compositional difference between the C- and B-type classes is their spectral flatness and brightness: C-type objects are darker and possess a flatter, slightly reddish (increasing) spectral slope spanning the near-UV to the near-IR; B-type objects have greater albedos and have slight bluish (decreasing) spectral slopes from the near-UV toward the near-IR (Bus & Binzel 2002a, 2002b).

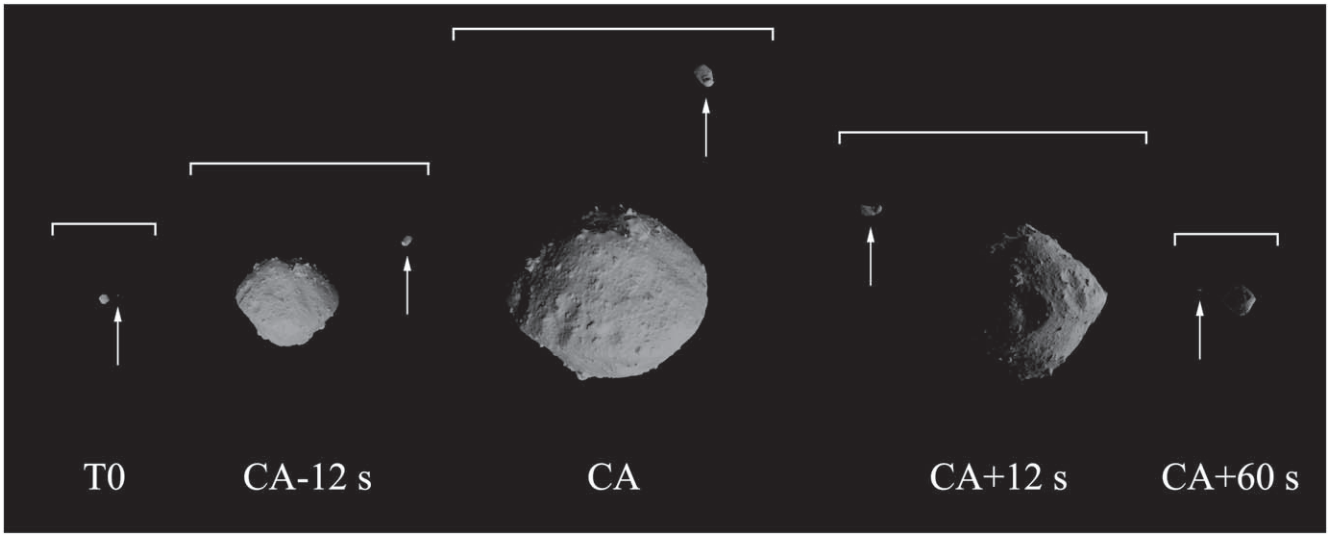

Figure 3. The LEIA simulated images obtained at *T0*, 12 s before LICIACube CA, at CA, 12 s after CA, and 60 s after CA. As for the DRACO simulated images, Didymos is represented by the scaled shape model of Ryugu, while Dimorphos is the scaled version of asteroid Itokawa. The white arrows point at Dimorphos in all panels. All images show the real targets' dimensions in the LEIA 2048 × 2048 detector.

the extremely blocky nature of the surface, with the largest boulders on Itokawa, Ryugu, and Bennu being between more than 1/10 the diameter of the asteroid: This suggests an interior clast size distribution that extends throughout the body. Furthermore, comparisons of the largest block size to the largest crater size on these asteroids reveal that their large block population was likely inherited from a catastrophically disrupted parent body (DellaGiustina et al. 2019). Moreover, porosities of around 30%–50% are also necessary for such rubble piles, according to the material compositions of these bodies, although what fraction is macroporosity (e.g., rubble) versus microporosity (dust or petrological voids) remains an open question (e.g., Consolmagno et al. 2008). A recent analysis of the returned samples from Ryugu shows that the sampled materials have a density of 1282 kg m^{-3}, similar to its bulk density, 1190 kg m^{-3}, implying a high microporosity and low macroporosity on this asteroid (Pilorget et al. 2022; Yada et al. 2022). This is in contrast to Itokawa, where macroporosity is high (39%) and microporosity is low (Tsuchiyama et al. 2014). For the case of Bennu, Walsh et al. (2022) and Lauretta et al. (2022) suggested that the asteroid's near-surface is underdense relative to the deeper interior.

These findings indicate the possibility of a strong contrast in internal porosity characteristics from asteroids of different taxonomic classes and have important implications on what we might expect on Didymos and Dimorphos. It is indeed likely that Didymos, with its top shape and rapid rotation, is a rubble-pile object originating from collisions (e.g., Zhang et al. 2021), implying a granulated, gravitationally bound remnant of a larger parent body. On the contrary, there are multiple hypotheses for the formation and evolution of Dimorphos, which is closer to the ∼100 m diameter transition to monolithic behavior suggested by collisional modeling (Benz & Asphaug 1999), asteroid rotation rates (the so-called "spin barrier"; see Harris et al. 2009), and mass shedding or fission from a fast-spinning primary (Walsh & Jacobson 2015).

Telescopic observations have suggested that about 16% of the NEAs may be binaries, i.e., larger primaries having smaller or similar-sized secondaries (Margot et al. 2002; Pravec et al. 2006; Margot et al. 2015). Walsh & Jacobson (2015) showed that among 117 observed binary asteroids, 88 asteroids (∼75% of the sample) have primaries less than 20 km in diameter and relatively small secondaries ($0.1 \leqslant$ secondary size/primary size $\leqslant 0.6$) orbiting within 9 primary radii. The Didymos–Dimorphos system is within this major group. The hypothesis of their formation is that fast-spinning primaries experience mass ejection, developing secondaries orbiting them, although other mechanisms such as impacts (mainly for large asteroids with small satellites, e.g., Durda et al. 2004; Richardson & Walsh 2006) and planetary tides (e.g., Bottke & Melosh 1996; Walsh & Richardson 2006; Fang & Margot 2012b) are also possible. The rotational origin stems from mass ejection and fission from primaries due to the Yarkovsky–O'Keefe–Radzievskii–Paddack (YORP; Rubincam 2000) effect (Scheeres 2007; Walsh et al. 2008; Jacobson & Scheeres 2011a). A series of observations detecting fast-rotating primaries (e.g., Pravec et al. 2006; Pravec & Harris 2007) supports a rotational-driven origin and may also explain the ubiquity of top shapes among the primary components of binary asteroids (e.g., Descamps & Marchis 2008; Benner et al. 2015). If the formation of Dimorphos is related to the top shape and rapid spin-up of Didymos by the YORP effect, where the material is spun off (Scheeres 2007; Walsh et al. 2008; Jacobson & Scheeres 2011b; Tardivel et al. 2018), then it, too, could be a rubble pile. Conversely, in the fairly unlikely case where Dimorphos is a remnant from a parent-body disruption event that has yet to reaccumulate, it might be a large individual boulder not that dissimilar to some of the largest boulders observed on the surface of Itokawa (longest dimension, $l \sim 50$ m; Abe et al. 2006), Ryugu ($l \sim 160$ m; Watanabe et al. 2019), and Bennu ($l \sim 92$ m; Daly et al. 2020a).

3.2. How Can the Geological Features of Didymos and Dimorphos Hint at the System Formation and Evolution?

It is worth highlighting that the observed geologic conditions identified on Didymos and Dimorphos may directly correlate with the system formation and evolutive mechanisms. As discussed above, there may be four possibilities that contribute to a satellite formation: (i) planetary tides, (ii) original moon

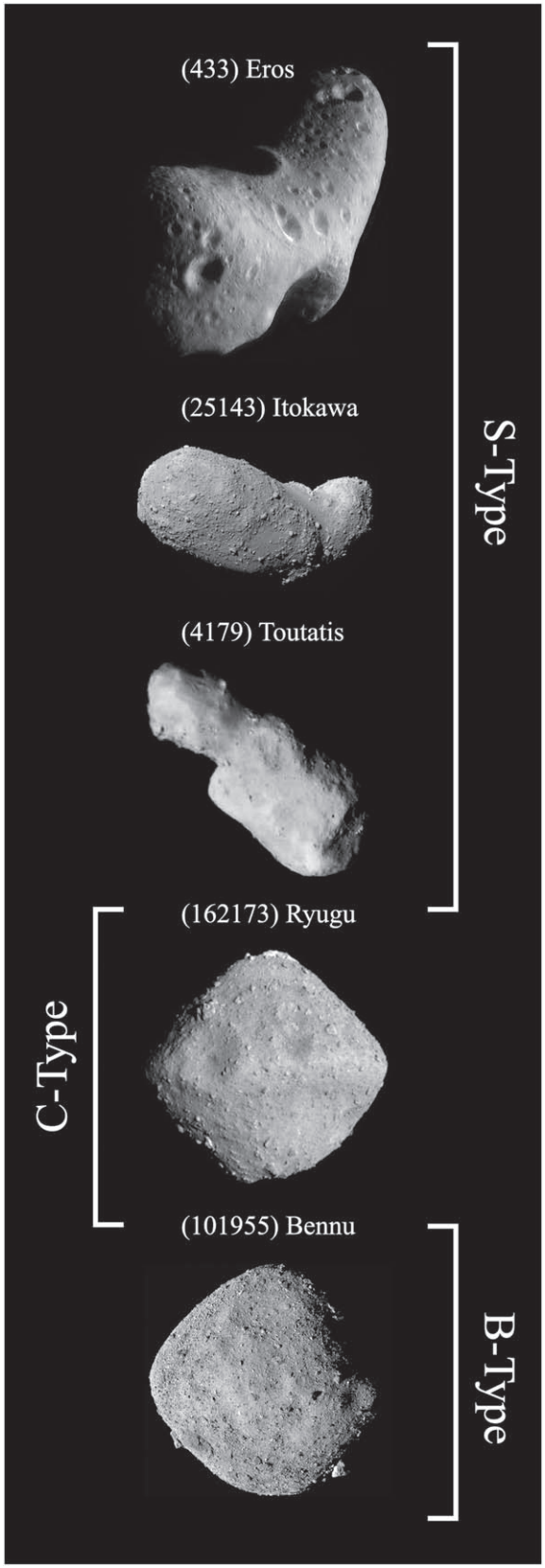

Figure 4. The five NEAs observed from close range so far. Asteroids Eros ($34 \times 11 \times 11$ km size), Itokawa ($0.5 \times 2.9 \times 2.1$ km), and Toutatis ($4.8 \times 2.4 \times 2.0$ km) belong to the same S-type class as asteroid Didymos. Ryugu ($1.04 \times 1.02 \times 0.88$ km) is a C-type asteroid, while Bennu ($0.57 \times 0.54 \times 0.51$ km) belongs to the B-type class.

from parent-body disruption, (iii) impact processes, and (iv) the primary's rotational effect.

By taking into account the current radar (Naidu et al. 2020) and light-curve data (Pravec et al. 2016), it is possible to eliminate planetary tides as a relevant mechanism for the formation and evolution mechanisms of Dimorphos. Indeed, tidal force makes the precursor body stretch, leading to the generation of elongated bodies. On the contrary, according to the radar-driven shape model (Naidu et al. 2020), Didymos is almost axisymmetric, hence contradicting the expected shape driven by planetary tides (Bottke & Melosh 1996; Walsh & Richardson 2006). The most recent light-curve analysis suggests a slightly smaller, more spherical, and denser object (Pravec & Scheirich 2022).

Regarding the impact scenario, the existence of large craters on Didymos may be one potential indicator. If Dimorphos turns out to be a monolith, the impact scenario is ruled out as block size-to-crater size scaling relationships suggest that a 10 km diameter crater is needed to generate a Dimorphos-sized monolithic boulder (Lee et al. 1996). The original disruption of a parent body leading to a primary and a monolith secondary might be in play (Michel et al. 2001; Durda et al. 2004), although ages derived from cratering would need to be consistent with a very young age for Didymos. On the other hand, if impact events were subcatastrophic, where a target having an impact may not exhibit a clear crater morphology but experience significant reshaping (Stickle et al. 2022), there may not be a singular indication of craters. In this case, a large amount of mass may be ejected from Didymos at lower ejected speeds (Perry et al. 2022), possibly contributing to the formation and evolution of Dimorphos. If this is the case, Didymos would have significant asymmetric topographic features. It is also likely that there exist boulders with different origins; in other words, the asteroid may host exogenous materials (DellaGiustina et al. 2021). In addition, it is also possible that the boulders' morphological conditions may differ depending on the impact conditions.

Didymos's 2.26 hr spin period leads to a surface slope that exceeds the typical friction angle of an angular granular material ($\sim 35^{\circ}$; Lambe & Whitman 1969) at low latitude regions (Zhang et al. 2017; Naidu et al. 2020). This spin period may be short enough to induce reshaping on various length scales: from mass movements on a local surface to global reconfiguration (Hirabayashi et al. 2014; Naidu et al. 2020; Zhang et al. 2021; Richardson et al. 2022). Rotational-driven reshaping would generate massive debris. Significant reshaping processes may be less frequent but can generate large mass ejections. On the other hand, small events may often occur in mechanically weak regions, particularly top surface layers. This likely explains the evidence for surface creep (Jawin et al. 2022), captured by tumbling rocks and terraces seen on Bennu (Barnouin et al. 2022), and can lead to additional distinguishable geologic units such as different color units and regional variations in boulder size-frequency distributions (SFDs). Ryugu, for example, exhibits latitudinal variegation in color that is consistent with mass flows toward its midlatitudes, the geopotential low on the asteroid (Sugita et al. 2019). Besides the evidence for surface creep, Bennu also has relatively dynamic mass flows on its entire surface (Daly et al. 2020a; Jawin et al. 2020). Similar features on Didymos would be

indicative of active mass flow on the asteroid that may have led to the formation of Dimorphos.

The rotational effect stems from mass ejection due to centrifugal forces because of Didymos' short spin period. In this case, depending on the existence of cohesion, the formation of Dimorphos may be different. If there exists cohesion, a chunk (or a monolithic rock) could have departed from Didymos (Jacobson & Scheeres 2011b; Jacobson et al. 2016; Tardivel et al. 2018). It is unclear what this process would leave behind, as large boulders on small asteroids are often well buried and not easily movable (e.g., Daly et al. 2020a). Maybe an equatorial cavity that does not have a typical crater aspect ratio and no evidence for raised rims is something to look for (Daly et al. 2022a). If particles are not cohesive (Lauretta et al. 2022; Walsh et al. 2022), shedding followed by reaccumulation may lead to satellite formation (Walsh et al. 2008, 2012).

For the latter cohesionless scenario, the two asteroids would have a similar material composition, but the presence of fine (<1 cm) regolith might be different. Solar radiation pressure may have enough time to blow away smaller particles (with sizes of ∼micrometers), depending on the orbital migration timescale from Didymos. The orbital evolution of ejected particles from Didymos to Dimorphos may result in the Dimorphos edge facing Didymos being fresher than the other edge if the mutual orbit is indeed in a dynamically relaxed state (Agrusa et al. 2021).

The observed surface geology may also depend on the evolution of mutual orbits between Didymos and Dimorphos. For example, Dimorphos' mean anomaly acceleration was reported to be small, inferring two scenarios. First, if this negligible anomaly acceleration results from Dimorphos chaotic motion, given limited binary YORP (called BYORP), thermal radiation causing the perturbation of the mutual dynamics, Dimorphos' surface may chaotically face Didymos, allowing it to have Didymos' material accumulations anywhere. In this scenario, a potential geologic scenario is that there are similarly aged materials all over the surface of Dimorphos. The second scenario is that while BYORP is indeed significant, the tide from Didymos on Dimorphos is also significant but canceling out the BYORP effect (Jacobson & Scheeres 2011a). In this case, Dimorphos' one side always faces Didymos, possibly giving a dichotomy in color between the facing direction and the other side. Any surface fracture seen in Dimorphos that is not associated with a given impact on Dimorphos but is circumferential to the secondary could be an indication of strong tidal effects, such as those seen on Phobos (Thomas & Prockter 2010).

4. Multiscale Mapping Strategies to Assess the Geological Character of Didymos and Dimorphos

To address some of the aforementioned plausible origins of Dimorphos, we plan to undertake a range of mapping efforts to assess the geology of both Dimorphos and Didymos. The images collected at Dimorphos and Didymos will allow the identification of different morphological units, as well as geological features such as craters, mass movements, boulders, fractures, and lineaments, together with the associated formative and degrading processes that occurred and/or are still occurring on the surface of the binary system. Here, we describe the mapping strategies using the DRACO, LEIA, and LUKE data of the targets and the type of geological features we will be looking for to understand them, though keeping in mind that (i) we have never visited an NEA binary system, and (ii) until arrival, we can only speculate on the targets' surface properties. We will make use of global shape models (Daly et al. 2022a), surface slopes, and high-spatial-scale images to provide, to the extent that the data allow, a preliminary detailed physiographic understanding of the interaction between Didymos and Dimorphos and gain insights into the interior properties that may influence the outcome of DART's impact. Hera is expected to update these findings.

4.1. Regional Classification and Impact Site Morphological Mapping

A fairly complete assessment of major morphological, topographical, and textural boundaries on the illuminated regions of Didymos and Dimorphos will be identified once DRACO and LEIA observe the two asteroids. After the first decameter-scale images of both asteroids become available, attempts will be made to divide the surface of both targets into regional units. It is important to quickly understand if there are evident morphological boundaries on the two NEAs and evaluate the possible stratigraphy of the derived units (as done on asteroid Bennu; Jawin et al. 2022). Such an approach was found feasible for asteroids Itokawa (Fujiwara et al. 2006) and (21) Lutetia (Massironi et al. 2012; Thomas et al. 2012; Figures 5(A) and (B)), and for comet 67P/Churyumov–Gerasimenko (El-Maarry et al. 2015), but it was much more difficult for asteroids such as Eros (Veverka et al. 2001), (243) Ida (Sullivan et al. 1996), and (951) Gaspra (Carr et al. 1994), where easily separable units were difficult to distinguish without additional analyses. In the first three cases, it was possible to distinguish, when present, "smooth terrains," i.e., surface areas that appear to be composed of fines, from "rough consolidated terrains," i.e., units that are characterized by a rocky and boulder-rich appearance. In the cases where textural structures were not immediately apparent, further analyses do eventually allow the identification of distinctive coherent regions based on textural, morphological, albedo, and topographical boundaries. Indeed, in the most pathological of cases, the rough rubble-pile asteroids Bennu and Ryugu, morphological similarities have been identified (Miyamoto et al. 2019; Jawin et al. 2021; Barnouin et al. 2022; Jawin et al. 2022) and proved to be useful to evaluate the stratigraphic relationship of the identified terrains.

Broad asteroid-wide regional unit classification of the observed portions of Dimorphos will be achieved with the low-resolution images (meter to decameter scale) from DRACO and LEIA. These units will be updated and refined with DRACO's highest-resolution data (but covering only specific parts of Dimorphos' surface), as well as complemented by LEIA observations of the nonimpacted side of the asteroid, through an iterative process making use of all the geological surface characteristics available. This effort will highlight broad-scale morphological asymmetries that the images and shape may divulge, hence hinting at how material from Didymos reached Dimorphos. However, the limited imaging coverage provided by DART and LICIACube will limit these assessments along the *X*-axis of Dimorphos.

To complement the regional unit classification of Dimorphos, we will use the highest-spatial-scale images (<0.5 m pixel^{-1}) and the derived topography obtained by DRACO to identify the different units of the final impact site, hence separating any

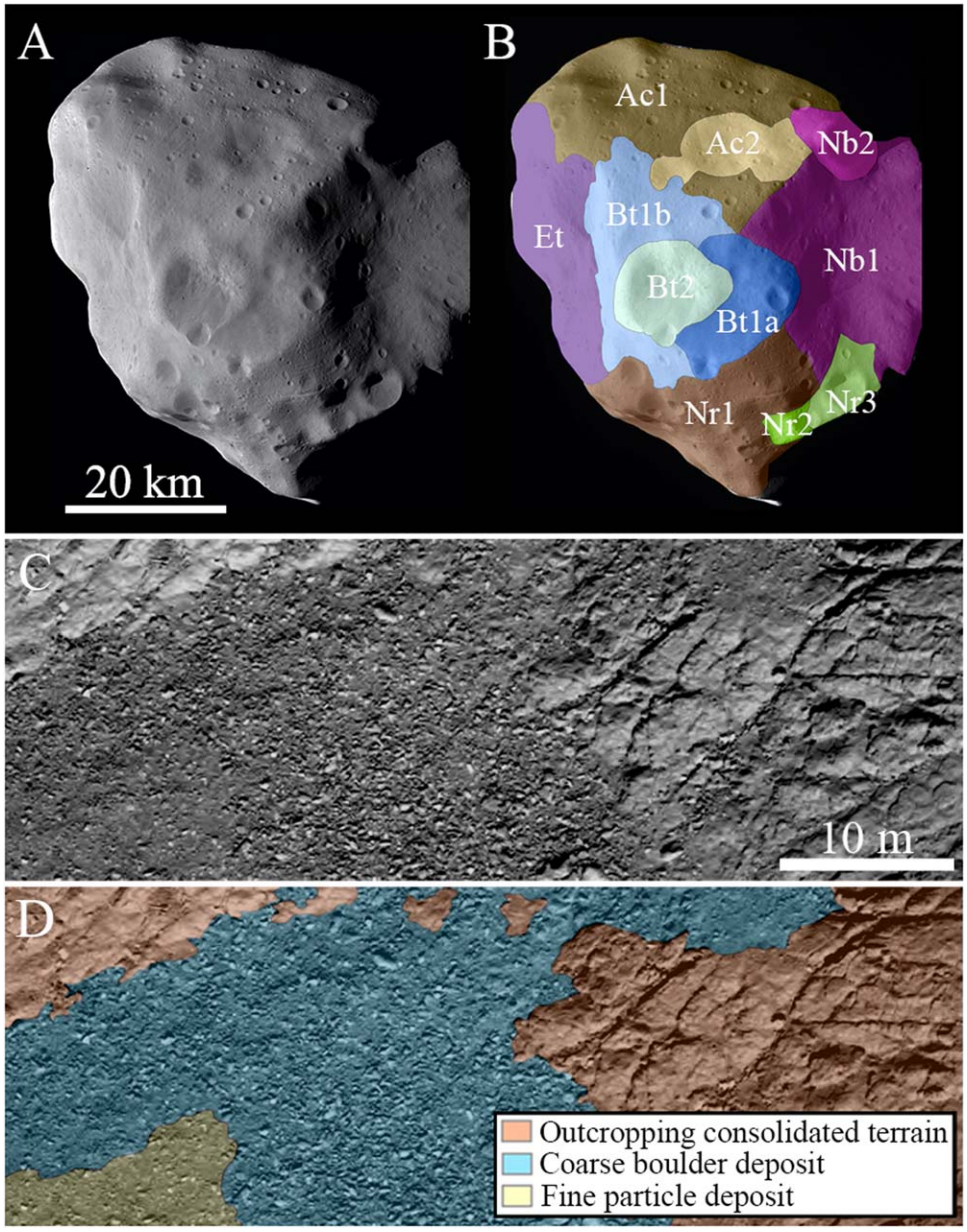

Figure 5. (A) Uninterpreted image of asteroid Lutetia as observed on 2010 July 10 by the OSIRIS camera on board Rosetta (Sierks et al. 2011). (B) Regional geological mapping obtained in (A). For the description of each geological unit (Achaia—Ac, Noricum—Nc, Narbonensis—Nb, Etruria—Et, Baetica—Bt), we refer to Massironi et al. (2012). (C) Uninterpreted image of the Rosetta Sais landing site on comet 67P/Churyumov–Gerasimenko (Sierks et al. 2015) taken on 2016 September 30 a few seconds before landing. (D) Geological map of (C). For a detailed description of each geological unit, we refer to Pajola et al. (2017a).

smooth, fine-particle deposit from consolidated, boulder-rich terrains (Figures 5(C) and (D)). By understanding the stratigraphic relationship of such units, we will therefore provide hints on the relative ages, as done, for example, on asteroid Bennu (Jawin et al. 2022). All resolvable craters present on site will be identified, too, assessing their spatial density and SFD. These high-resolution images should also permit the identification of surface linear features (if any) such as fractures and strata, hence deriving their orientation in space to infer any possible subsurface weakness or layering of the crash site. In addition, through the help of their localized shadows, the boulder SFD located on site and their morphologies including cracks will be identified, providing hints on how micrometeorites and/or thermal stresses might affect the area. The merger of all such information will be key to assessing the morphological nature of the DART impact site and possibly Dimorphos' nearest subsurface, hence providing important data for any efforts to model the DART collision (e.g., Stickle et al. 2022).

4.2. Color Differences/Variegation on the Surface

The geological mapping efforts are greatly aided by the use of color data provided by LICIACube/LUKE. This multicolor image data set will provide clues to the potential variegation in the surface composition of the binary system (see Poggiali et al. 2022), similarly to what was achieved for the S-type asteroids Ida and Dactyl (Figure 6), where data were collected during a flyby (Geissler et al. 1996). These color data converted into spectrophotometry measurements are related to several surface

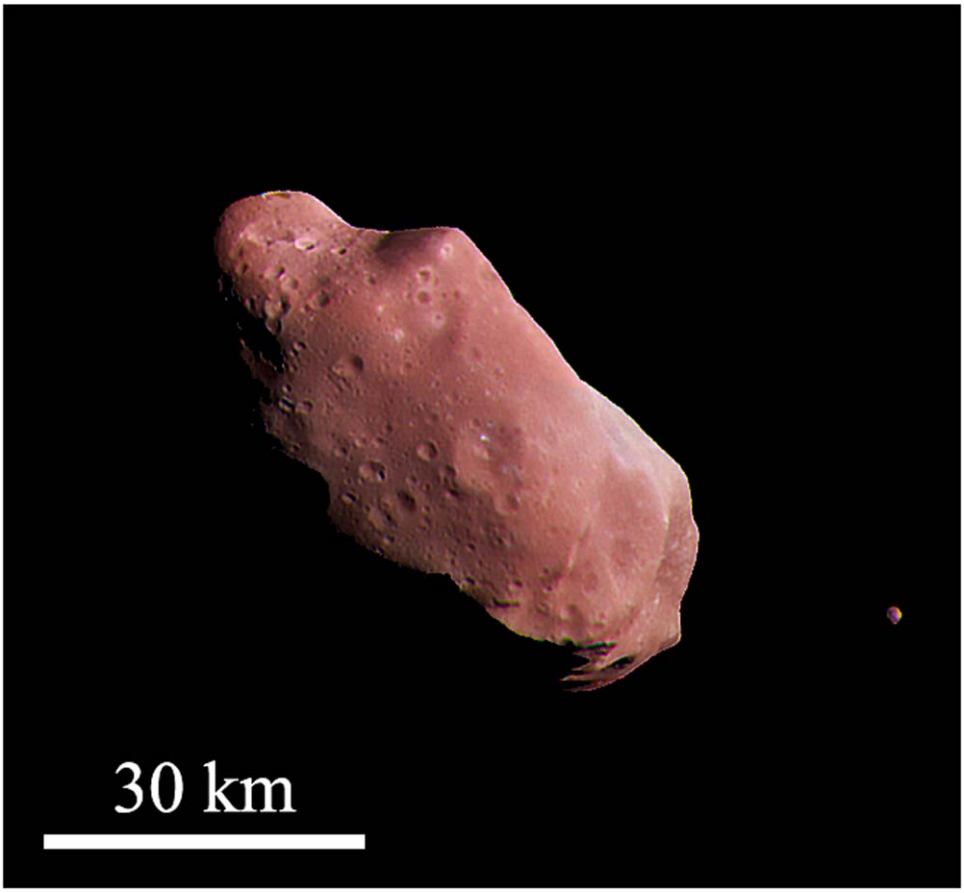

Figure 6. An enhanced-RGB color image obtained on the S-type asteroid Ida and its satellite Dactyl, as obtained by the Galileo mission on 1993 August 28. Thanks to such a data set, a systematic difference between two of Ida's major color terrains has been identified (Geissler et al. 1996; Veverka et al. 1996), as well as a different spectral trend on Dactyl.

properties, such as space-weathering alteration (e.g., Murchie et al. 2002; DellaGiustina et al. 2020; Rizos et al. 2021). The comparison of any spectrophotometric trends to laboratory analog samples will lead to insights into the surface mineralogy of the studied targets (Poggiali et al. 2021).

In addition, the study of RGB color data through the multivariate statistical clustering technique (e.g., Perna et al. 2017) will help to assess any possible localized heterogeneity or uniformity of Dimorphos and Didymos, mapping mineralogical differences and the presence of potential exogenous material, as observed in the case of Bennu and Ryugu (DellaGiustina et al. 2021; Kaplan et al. 2020; Tatsumi et al. 2021), and may provide evidence for material from other taxonomic classes of asteroids. Moreover, this will be important to confirm whether or not the spectral variations on Didymos suggested by ground-based observations (Ieva et al. 2022) match.

Eventually, DART's impact may act in favor of revealing more pristine material beneath the surface of Dimorphos in the ejecta produced during the DART kinetic impact event. LUKE has some chance of observing color differences while the DART crater forms, providing an opportunity to see the fresh interior of Dimorphos and to study how an S-type surface may have been affected by evolutionary processes, as demonstrated by the impact experiment performed by Hayabusa2 on the carbonaceous NEA Ryugu (Honda et al. 2021).

4.3. Geological Processes and Features

The preparation of geological maps of Dimorphos and Didymos requires an understanding of the range of processes these objects might experience. Below, we review the possible manifestation of these geological processes and summarize some of the items we will pursue in our investigation of this binary system.

4.3.1. Crater Statistics and Morphology

Impact craters are ubiquitous on asteroids (Figure 7) and provide a means for characterizing an asteroid's surface history and its near-surface and interior properties. As the population and flux of impactors in the near-Earth environment are well understood (Brown et al. 2002; Ivanov 2006), the surface age of Didymos and Dimorphos, as informed by the population of impact craters, can be obtained once the strength of the surface is measured by the DART experiment. The surface age of a rubble-pile asteroid places a constraint on the time of its formation through the catastrophic disruption of its parent body (Michel et al. 2009; Sugita et al. 2019; Walsh et al. 2019) or could be indicative of its last major resurfacing event (Asphaug 2009). Independent of a direct determination of the absolute surface age for both asteroids, a relative surface age between Didymos and Dimorphos can be obtained by comparing their respective crater densities (e.g., Melosh 1989), accounting for possible differences in crater scaling

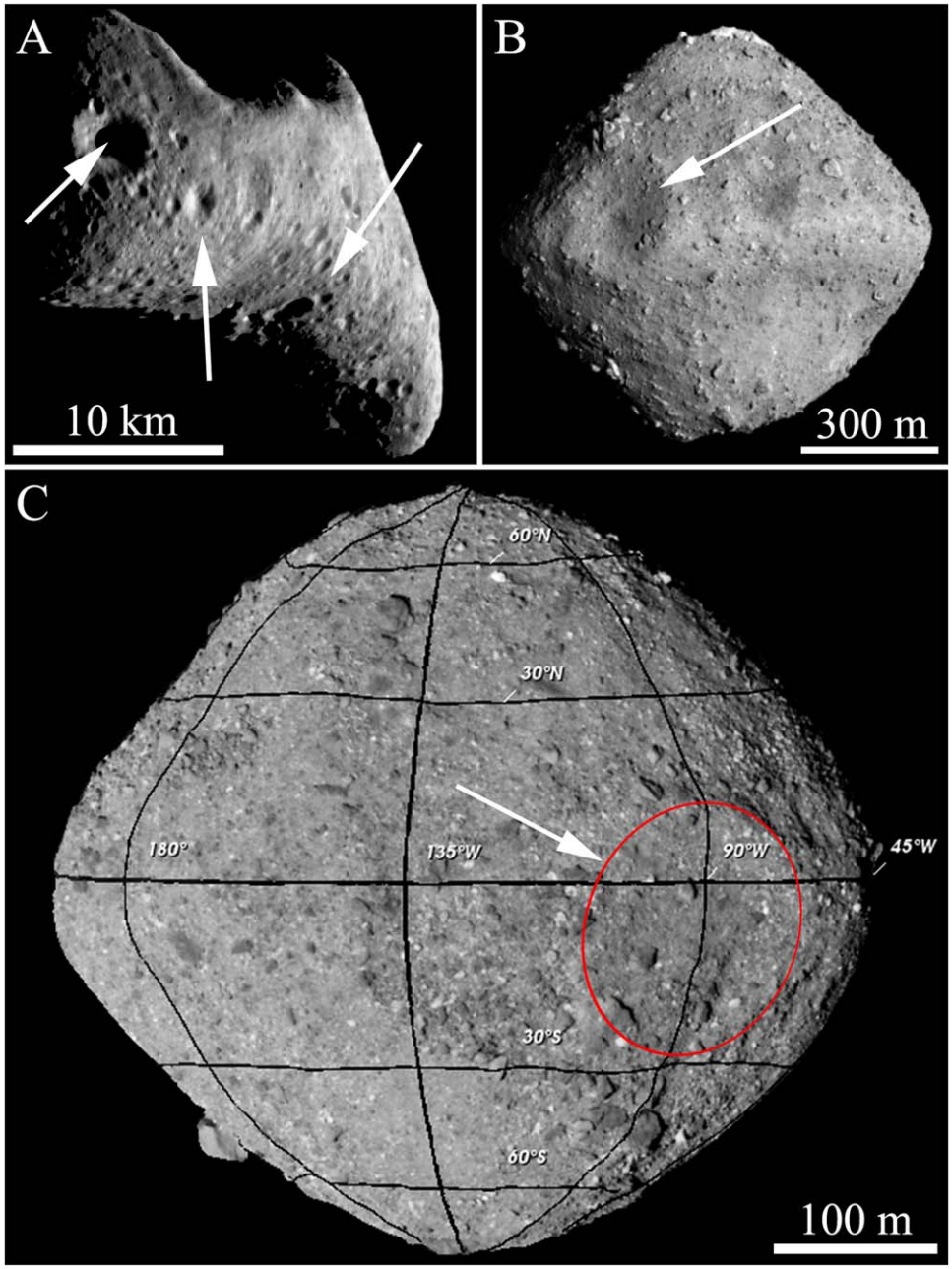

Figure 7. (A) The cratered surface of Eros, as imaged by the NEAR/Shoemaker spacecraft. White arrows point to the asteroid's multiple craters. (B) The surface of NEA Ryugu as observed by Hayabusa2. The largest crater identified on its surface is indicated with a white arrow. (C) An image of asteroid Bennu as observed by OSIRIS-REx draped over a low-resolution shape model in the Small Body Mapping Tool (Ernst et al. 2018). The largest equatorial crater is identified with a red circle and a white arrow.

due to the size and possible structural difference between the two components. If an observable difference is found in crater density between the two components of the binary, then crater statistics could inform the origin of the binary system, or it may be indicative of an active crater erasure mechanism that is more efficient on one of these bodies (e.g., Richardson et al. 2005; Bottke et al. 2020). Once the strength of the surface is measured, the crater statistics may also then provide an absolute timescale since the formation of the binary system, providing a crucial component to understanding the evolution of NEA binaries.

The surface age of an asteroid is typically constrained by its largest craters, which are hypothesized to vary depending on asteroid size and/or structural properties. For example, the main-belt asteroid (253) Mathilde (~50 km diameter) hosts several large and deep craters of up to ~60% of its diameter (Veverka et al. 1999). Housen et al. (1999) proposed that these craters are indicative of a compaction-cratering process that can occur on highly porous objects such as Mathilde, which has a low density of 1.3 $g\,cm^{-3}$. Alternatively, Asphaug (2008) proposed the size of the largest undegraded crater on an asteroid scale with asteroid diameter. A measurement of the size of the largest crater on the asteroid provides a way to characterize the asteroid's interior's ability to attenuate the seismic wave that resurfaced the asteroid. For Didymos and Dimorphos, the model of Asphaug (2008) would suggest that

the largest craters on their surface are expected to be ∼0.1× their size. If larger craters existed, this could be indicative of an interior with strong attenuation properties that could rapidly weaken a seismic wave before it is able to traverse the entire length of the asteroid.

Expectations from DART and LICIACube. Critical to understanding the surface properties and evolution of Didymos and Dimorphos through their crater population will be an assessment of crater morphology. Crater morphometrics help elucidate the structural properties of an asteroid and its surface evolution (e.g., Prockter et al. 2002; Daly et al. 2020b; Noguchi et al. 2021). For example, some large craters (>500 m in diameter) on Eros exhibit polygonal square shapes indicative of structural control (Prockter et al. 2002). On Bennu, some of the larger craters (>10 m in diameter) exhibit central mounding, indicating the possibility of subsurface strength (Daly et al. 2020a). In some special circumstances, large depth-to-diameter ratios for craters can indicate the presence of a highly porous interior (Housen & Holsapple 2003; Schultz et al. 2007; Nakamura 2017). Finally, the shallowing of craters can be indicative of mass wasting. Some characteristics, such as the presence of square craters, can be more directly assessed or measured than others, such as the depth of the craters. The expected limited stereo range from DRACO and LEIA images (Daly et al. 2022b) will make it difficult to construct detailed local terrain models of craters as has been done on Eros, Bennu, and Ryugu, for example (Ernst et al. 2012; Daly et al. 2020b; Noguchi et al. 2021). However, we expect to measure the depths of craters ⩾10 m in diameter using stereophotoclinometry (Gaskell et al. 2008; Barnouin et al. 2020; Palmer et al. 2022). We will also measure crater depths using shadow measurements, as was successfully done for Eros, if the surface is not rugged, which does not rely on generating topography. Indeed, Robinson et al. (2002) measured average depth-to-diameters of 0.12 from shadows, which is similar to what has been found via shape modeling (Ernst et al. 2012) and the use of Near Laser Rangefinder data (Marchi et al. 2015). Using shadows, we expect to be able to measure the depths of craters up to a few meters in size. Thus, we expect that an intra-asteroid comparison of crater depth-to-diameter ratios (*d/D*) could provide insight into either structural or surface age differences between Didymos and Dimorphos. Moreover, an intra-asteroid comparison of *d/D* would probe region-specific variations of the near-surface (e.g., boulder population and possible impact armoring, Bierhaus et al. 2022), the subsurface (e.g., presence of mascons), or surface evolution.

4.3.2. Mass Wasting/Movements

Various forms of mass wasting have been observed in the solar system, not only on Earth but also on multiple other bodies, such as the Moon (e.g., Bart 2007; Xiao et al. 2013), Mars (e.g., Crosta et al. 2018; Pajola et al. 2022), Mercury (e.g., Malin & Dzurisin 1978), Venus (e.g., Malin 1992), the Martian moon Phobos (e.g., Shi et al. 2016), Jovian moons (e.g., Schenk & Bulmer 1998; Moore et al. 1999), Saturnian moons (e.g., Singer et al. 2012), and Charon (Beddingfield et al. 2020). In addition, mass-wasting features have also been detected and investigated on the surfaces of minor bodies, such as on comets and asteroids (e.g., Figure 8(A), (B); Sullivan et al. 1996; Thomas et al. 2002; Miyamoto et al. 2007; Barnouin-Jha et al. 2008; Massironi et al. 2012; Pajola et al. 2017b; Schmidt et al. 2017; Barnouin et al. 2019; Lucchetti et al. 2019; Walsh et al. 2019; Daly et al. 2020a; Jawin et al. 2020; Barnouin et al. 2022). These investigations reveal that one can get a broad range of surface characteristics associated with mass-transport events and their related accumulation deposits. The mechanism responsible for mass movement is controlled by different factors, such as the slope failure or the mechanical properties of the material. On small bodies, the occurrence of mass movements driven by rotation can play a dominant role in shaping regional surfaces, and maybe even their overall shape (e.g., Walsh et al. 2008). Detailed analysis of such events can provide insight into the mechanical behavior of their constituting material. For instance, high-resolution images of comet 67P/Churyumov–Gerasimenko allowed the characterization of the deposits originating from mass-wasting events that reveal a cometary material more akin to Earth dry landslides than to mass movements on icy satellites, despite the cometary composition (Lucchetti et al. 2019). Such geomechanical analyses are also possible on NEAs. On Bennu (Barnouin et al. 2022), evidence for ongoing surface creep and formation of observed surface terraces indicates that Bennu's top 8–10 m of unconsolidated surface material is very weak and likely has very little to no cohesion (<0.6 Pa). On Eros, bright and dark streaks have been identified as the results of downslope mass movements/landslides of mature regolith (Figure 8(B), Veverka et al. 2001; Thomas et al. 2002). Deposits of granular material have been observed at the base of slopes (Cheng 2002) suggesting that the asteroid surface is characterized by a regolith layer overlying a substrate with some competence several tens to hundreds of meters below the surface (Robinson et al. 2002). In the case of Itokawa, smooth terrains of loose small-sized granular material coincide with regions of low gravitational potential or elevation (Miyamoto et al. 2007; Barnouin-Jha et al. 2008). Observations suggest transportation of these small-sized granular regolith particles by seismic shaking, thermal processes, and/or tidal effects that gradually cover up the boulder-rich terrain (Miyamoto et al. 2007; Barnouin-Jha et al. 2008). The evidence that the regolith migration is a gravitationally induced motion is supported by gradual changes in surface roughness from the roughest high-standing terrains to the smoother low-lying regions (Barnouin-Jha et al. 2008; Susorney et al. 2019). It is also evidenced by the long axes of boulders oriented transverse to the direction of gravel migration, which consistently matches the local slopes (Miyamoto et al. 2007).

Features indicating mass wasting on Ryugu are in the form of crater wall slumping, showing the existence of unconsolidated particles, asymmetric regolith deposition on imbricated boulders, and an indication of boulders burial (Michikami et al. 2019; Sugita et al. 2019). On Ryugu, the mass movement's direction is in agreement with the current topographic profile and the geopotential of the asteroid (Sugita et al. 2019).

An impressive candidate mass movement deposit was first identified inside a large crater on Bennu's equator (Figure 8(C); Barnouin et al. 2019; Walsh et al. 2019). Smaller and asteroid-wide features were mapped by Jawin et al. (2020), identifying rock fragments of various sizes sitting on other boulders, boulder imbrication, and partly buried boulders. Such features have been observed at different scales ranging from meter scale, as individual boulders, to the aforementioned single ∼100 m-long debris flow. In all cases, their movement is consistent with the local downslope direction (which is generally oriented N–S toward the equator, Jawin et al. 2020). Daly et al. (2020a) show that the existence of ancient but pervasive mass movements on the northern hemisphere of Bennu and their absence in the south may in part explain the hemispherical shape difference seen at

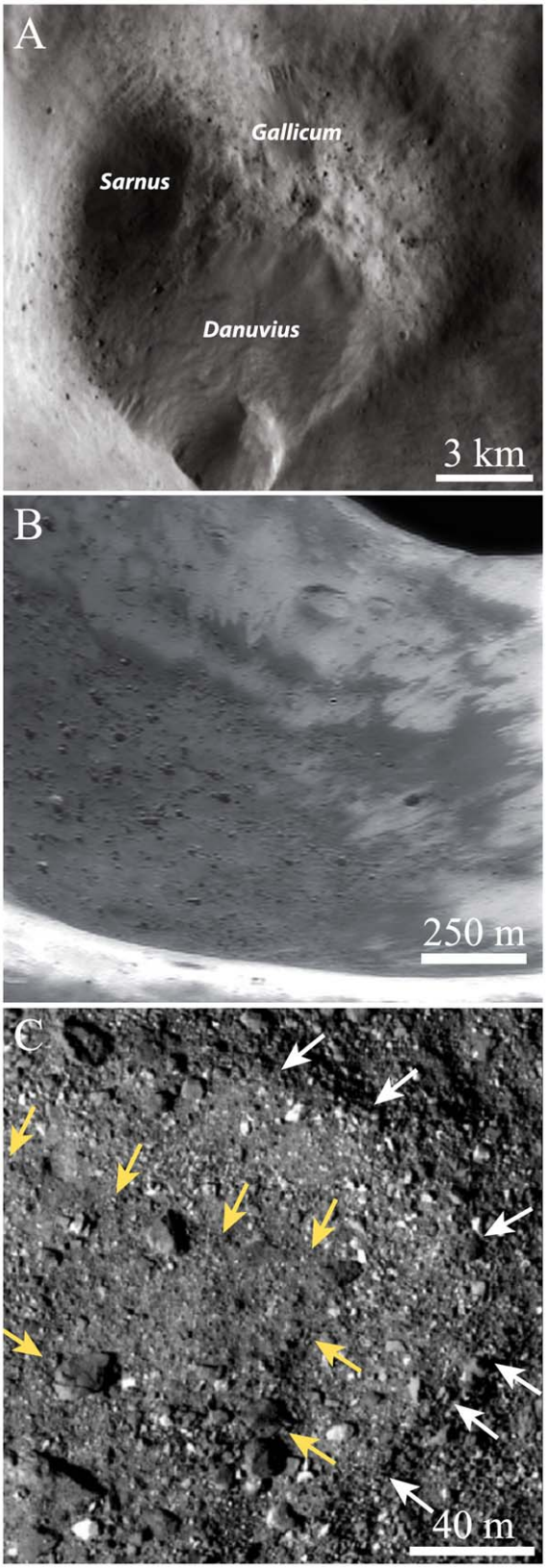

Figure 8. (A) Three landslides (named Sarnus, Gallicum, and Danuvius) observed on the surface of asteroid Lutetia (from Massironi et al. 2012). (B) Mass movement examples as observed inside the Psyche crater on Eros. (C) The single ∼100 m-long mass movement (highlighted with the yellow arrows) is observed on the surface of Bennu (Jawin et al. 2020), entering a crater (the rim is indicated with white arrows).

Bennu. Due to the continued spin-up of the asteroid and the resulting steepening of its surface slopes, mass movements are expected to continue occurring on the surface of the NEA (Jawin et al. 2020). Currently, surface creep is ongoing, resulting in the formation of terraces, as well as the toppling of boulders (Barnouin et al. 2022). This includes reorientation of the long axis of boulders both parallel (for boulders that slide into position) and perpendicular (for boulders that roll) to the slope direction (Barnouin et al. 2022).

Expectations from DART and LICIACube. The DART and LICIACube images will provide an opportunity to enhance our understanding of mass movements affecting the surface of NEAs and, in particular, those on the surfaces of objects in a binary system. Indeed, we expect to detect and investigate several features related to mass movements, such as the presence of variable boulder concentration, organized boulders, and possibly imbricated boulders. We may even see topographic evidence of creep-driven terracing and surface flows. In some cases, the downslope direction of mass movements and the resulting surface expression can change depending on the asteroid rotation velocity, which changes over time, while in other cases impacts on the surface of an asteroid can induce seismic shaking that results in downslope motion of loose, unconsolidated material. Roughness changes with surface elevation not only provide clues to surface displacements by mass movements, but they can also provide evidence for how asteroid landscapes evolve over time due to, for example, changes in spin rates (Susorney et al. 2021). Determining the triggering mechanism for mass movements from DART and LICIACube observations is key to providing information about the surface properties of the regolith that DART may encounter. As discussed in Section 3, evidence for mass movements on Didymos feeds directly into our understanding of the evolution of binary asteroids and similar fast-rotating bodies.

The tidal interaction between Didymos and Dimorphos may also contribute to mass movements on either object (Zhang et al. 2021) as well as mass exchange between the two. Evidence for longitudinal or latitudinal variations of surficial mass concentrations will be critical to assess, to aid in understanding how any of the tidal interactions may obscure insight into the origins of Dimorphos. We do predict that variations will exist in part as a consequence of Dimorphos' likely spin-locked state.

4.3.3. Boulders

In 1965, the first unearthly boulders were revealed on the lunar surface thanks to a wealth of photographs obtained by a large number of spacecraft (Kuiper 1965). In 1977, the Viking landers photographed Martian boulders (Mutch et al. 1977), suggesting that they might be ubiquitous on solid planetary surfaces. From that moment on, the increasing resolutions of the images of planetary surfaces led to the possibility of acquiring the SFD of boulders present on the solid surfaces of all explored solar system bodies.

Today, the boulder SFD analysis is a widely accepted and used tool to test and investigate some of the geomorphological processes that shaped a planetary surface (e.g., Grant et al. 2006; Yingst et al. 2007; Golombek et al. 2008; Yingst et al. 2010; Pajola et al. 2017c, 2022). This approach is not only used for planets, indeed there is increasing literature documenting

the SFD of boulders on minor bodies and satellites such as the Martian Phobos and Deimos (e.g., Lee et al. 1986); on asteroids (243) Ida (Geissler et al. 1996), (433) Eros (Thomas et al. 2001), (25143) Itokawa (Michikami et al. 2008; Mazrouei et al. 2014), (21) Lutetia (Küppers et al. 2012), (4) Vesta (Schröder et al. 2020), (101955) Bennu (Daly et al. 2020a; Burke et al. 2021), and (162173) Ryugu (Michikami et al. 2019); on the dwarf planet Ceres (Schröder et al. 2021); on the Moon (Bart & Melosh 2010); on Enceladus (Pajola et al. 2021); and, more recently, on cometary nuclei, such as 67P/Churyumov–Gerasimenko and 103P/Hartley 2 (Pajola et al. 2015, 2016a, 2016b).

As previously mentioned, small asteroids (<10 km) are commonly considered to be reaccumulated remnants from disrupted parent bodies (Ryan & Melosh 1997; Durda et al. 1997; Benz & Asphaug 1999; Walsh 2018; Delbo et al. 2019). Surface boulders, therefore, represent (i) directly the fragments of those parent-body disruptions, (ii) secondarily, the collisional evolution of those fragments subject to cratering and thermal breakdown on the surface of the small asteroid, and (iii) the size-sorting and migration of granular materials in the mobilized regolith of a small asteroid (e.g., Miyamoto et al. 2007). Hence, deriving the boulder SFD on the surface of an NEA and the corresponding power-law indices is a powerful tool for understanding their initial formation and subsequent evolution.

The two S-type NEAs Eros and Itokawa and the two carbonaceous/organic-rich C-type Ryugu and B-type Bennu have been imaged from meter to submeter resolutions, allowing the most detailed boulder SFD analyses ever performed on small bodies. Thanks to the NASA/NEAR mission to Eros, the collected images allowed Thomas et al. (2001) to detect ∼7000 rocks ⩾15 m over the entire surface, deriving a power-law index of the best SFD fitting curve of −3.2, while a later analysis allowed investigating ∼34,000 boulders ⩾1 m, deriving a comparable power-law index of −3.1 (Dombard et al. 2010). By using images of Itokawa, Michikami et al. (2008) identified nearly 5000 boulders larger than 1.6 m in diameter and a total of ∼490 boulders larger than 5 m (Figure 9(A)), getting a power-law index of -3.1 ± 0.1. A later analysis performed by Mazrouei et al. (2014) identified a power-law index of -3.5 ± 0.1 for all boulders ⩾6 m (Figure 9(B)).

In the mentioned works, the power-law index range of −3.1 to −3.5 has been thoroughly discussed as representative of an impact-related size distribution as validated by impact simulations on low-gravity bodies (Thomas et al. 2001; Michikami et al. 2008; Küppers et al. 2012; Mazrouei et al. 2014) and on the Moon (Shoemaker & Morris 1970; Bart & Melosh 2010).

On Ryugu, Michikami et al. (2019) identified nearly 4400 boulders ⩾5 m that appear to be uniformly distributed across the full surface, with some latitudinal and longitudinal differences. In particular, a lower number density in the equatorial region has been identified, while the resulting SFD of the entire surface is characterized by a power-law index of -2.65 ± 0.05. For Bennu, DellaGiustina et al. (2019) and Burke et al. (2021) counted a total number of 3136 boulders with diameters spanning between 1.3 and 58.4 m. The estimated completeness limit used to compute the global SFD is 8 m and the resulting power-law index is -2.9 ± 0.3. Nevertheless, multiple centimeter-scale images (Figure 9(C)) returned the possibility of counting more than 55,000 pebbles/boulders on the two sampling site finalists, deriving power-law indices ranging from -2.2 ± 0.1 to -2.7 ± 0.6 (Burke et al. 2021).

The boulders on Ryugu and Bennu are suggested to be the result of their larger parent bodies' disruption (Sugita et al. 2019; DellaGiustina et al. 2019); nevertheless, their SFDs are shallower when compared to the S-type NEAs. Watanabe et al. (2019) proposed that the past migration of small particles toward the equatorial ridge of such asteroids might have buried the smallest boulders, hence decreasing the power-law index value. This is supported by boulder counts performed on smaller areas and with higher-spatial-scale images, where the SFD gradually decreases with boulder size. This trend might also be present on Bennu (Burke et al. 2021); nevertheless, it is worth mentioning that the coupled thermal stresses (Molaro et al. 2020b) and micrometeorite bombardment (Ballouz et al. 2020) might affect more the smaller rather than the larger sizes, hence fully disintegrating them and shallowing the resulting global SFD.

Expectations from DART and LICIACube. If we take into consideration both the ∼60° phase angle images of DRACO, which is good for identifying surface features thanks to the presence of elongated shadows, as well as the three-pixel sampling rule (e.g., Michikami et al. 2008; Pajola et al. 2015), the DRACO image data set will be enough to count all boulders ⩾18 m visible in the illuminated hemisphere of Didymos, reaching dimensions ⩾10 m in some of its areas. For Dimorphos, we will be able to identify all boulders ⩾1.5 m on its visible surface, reaching minimum sizes ⩾0.2–0.3 m surrounding the DART impact location. This data set will be complemented by the LEIA images that will allow the identification of boulders ⩾4.5 m on the illuminated sides of Dimorphos and Didymos (6–7 m on the nonimpacted Dimorphos hemisphere, as well as on the Didymos side not observed by DRACO). Such identifications will be crucial to determine the boulder's SFD and compare it with the other NEA values, hence deriving their formation processes and morphologies. It is indeed not yet clear whether, despite similar disruptions and rubble-pile formations, as well as impact degradations, S-type objects commonly present steeper SFDs than carbonaceous asteroids or not. For the case of Didymos, which is an S-type NEA, one might expect a similar power-law index range to that of Eros and Itokawa if impacts modified its surface-generating boulders in a similar way. Nevertheless, because Didymos is top-shaped like Ryugu and Bennu, it might have experienced a similar equatorial pebble migration as explained by Watanabe et al. (2019), hence it could show a shallower SFD. In addition, Didymos is a binary asteroid, therefore any tidal interaction or particle exchange between the two bodies might have modified the original boulder SFD. This, in particular, is extremely important to be considered when the first results will be obtained. For Dimorphos, we do not know yet if it is a single monolithic body or a rubble pile itself that formed from Didymos: this means that until arrival, we can only speculate on the boulder SFDs we are going to derive and the corresponding boulder surface densities. Nevertheless, it is clear that the boulder SFD analysis will provide hints to answer these questions, hence returning crucial information on the system origin and surface modifications.

Lastly, throughout the DRACO and LEIA data sets, we might detect impact degradation that has happened to the largest boulders. This aspect is of great importance because the size of the largest boulder compared to the size of the largest crater is an important indicator of the formation of the system (catastrophic disruption) and its rubble-pile nature (DellaGiustina et al. 2019).

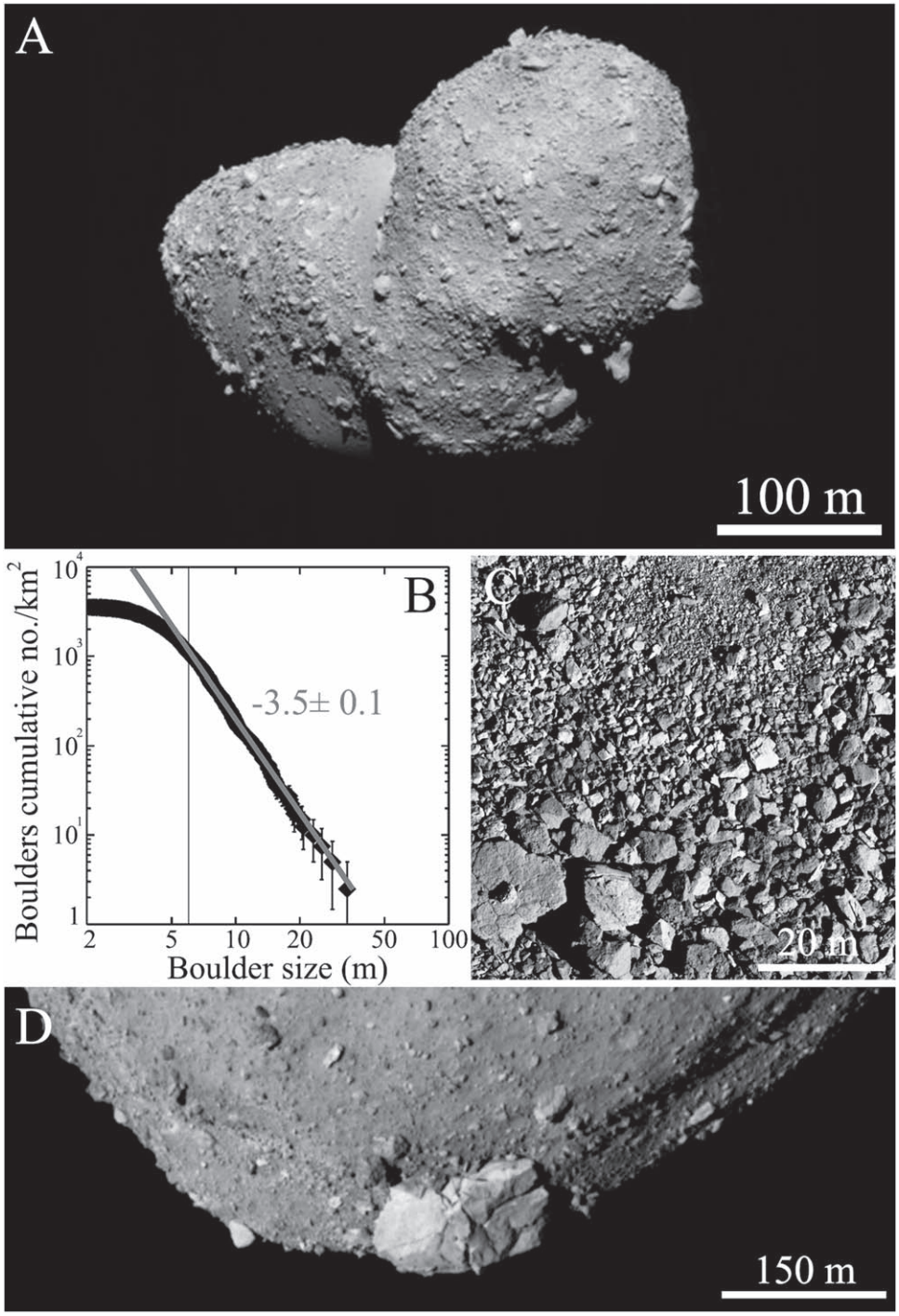

Figure 9. (A) The boulder-rich surface of NEA Itokawa, as observed by Hayabusa. (B) The Itokawa global SFD of boulders as obtained by Mazrouei et al. (2014). (C) Boulders' size grading on Bennu, as observed on a centimeter-scale OCAMS-Polycam (Rizk et al. 2018) image. (D) The southernmost region of asteroid Ryugu. The biggest boulder, called Otohime Saxum, has a size (160 m) that is comparable to the size of Dimorphos.

Moreover, the size of the largest boulder (as the 160 m-wide Otohime Saxum on Ryugu, Figure 9(D)) will be a necessary component for constraining the strength of monolithic asteroids (Ballouz et al. 2020), hence providing important implications for the targets' interior properties.

4.3.4. Fractures and Lineaments

Lineaments are common features that have been found on the surface of many asteroids and provide insights into the internal structure and history of the body (Veverka et al. 1994; Prockter et al. 2002; Sullivan et al. 2002; Besse et al. 2014; Marchi et al. 2015; Simioni et al. 2015). Linear features are usually identified in variable forms, such as ridges, troughs, grooves, and pit chains (Thomas & Prockter 2010). In many instances, primarily for larger asteroids (>30 km), lineament and groove orientation are associated with impact craters (Figures 10(A) and (B)) providing information about internal stiffness (Buczkowski et al. 2008; Marchi et al. 2015). Lineaments can also be the response to stress readjustment, while long linear

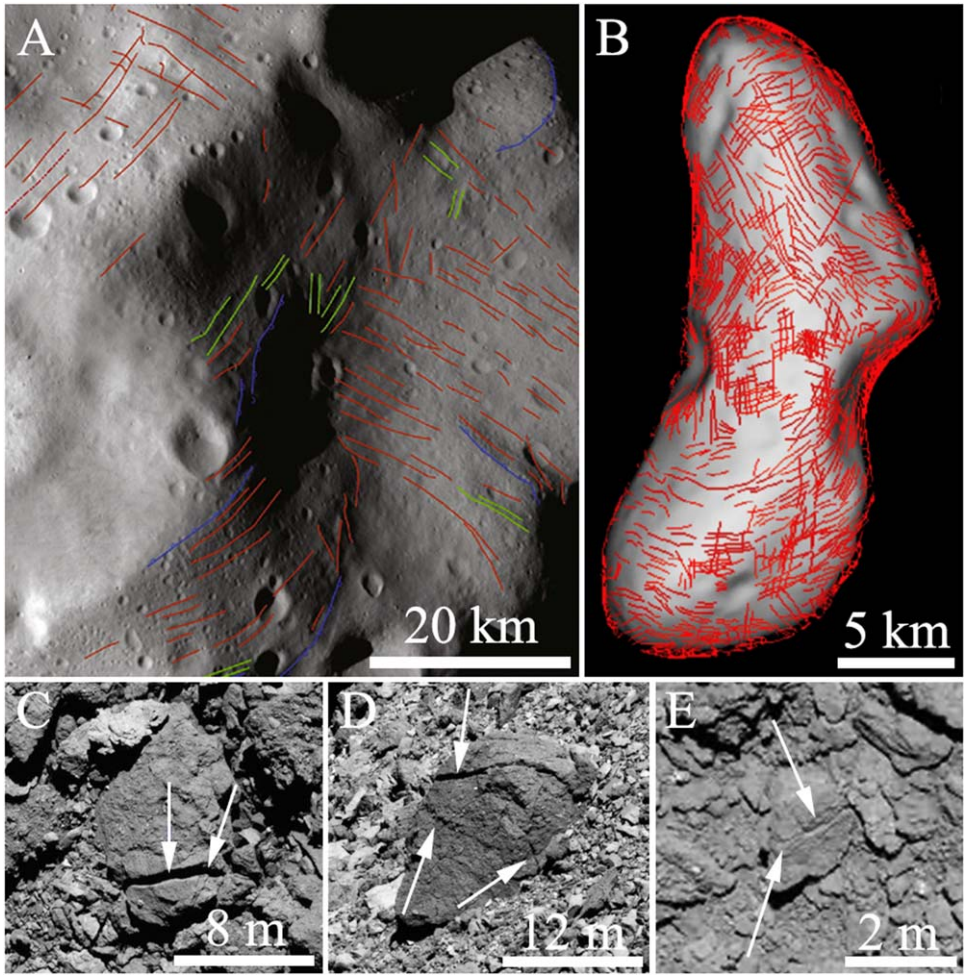

Figure 10. (A) Examples of kilometer-long grooves and lineaments on the surface of asteroid (21) Lutetia (from Massironi et al. 2012). (B) The global distribution of lineaments on NEA (433) Eros (Buczkowski et al. 2008). (C)–(E) Examples of linear through-going fractures on the Bennu boulders ((C), (D) Molaro et al. 2020a, 2020b) and on Ryugu ((E), Sasaki et al. 2019). The white arrows point out the identified fractures.

grooves are usually considered evidence of structural coherence (Barnouin et al. 2014; Marchi et al. 2015).

In order to understand the lineaments' formation process, it is important to know their 3D orientation and distribution, especially for small bodies. For instance, on Eros, lineaments were found to be ubiquitous at different scales and their formation of some lineament sets is clearly related to impact craters (Buczkowski et al. 2008; Figure 10(B)). However, there are some lineated sets that are not associated with craters. These may have formed during the disruption of Eros' parent body and provide hints that a broad regional boundary exists within the asteroid (Buczkowski et al. 2008; Buczkowski & Wyrick 2015).

In the case of the rubble-pile asteroid Itokawa, which does not have many impact craters on its surface, linear structures have also been identified (Sasaki et al. 2006; Cheng et al. 2007). Some lineaments may be the result of boulders movements whose presence does not require a coherent interior (Sasaki et al. 2006), while others have been observed to be confined to the body of the asteroid and could infer some localized coherence or at least an ability to transmit stress waves over a portion of the asteroid (Barnouin et al. 2014).

Despite its small size, Bennu possesses some lineaments (Barnouin et al. 2019) that may appear to be similar in density to the lineaments present on Eros, but with more concentration in the northern hemisphere (Perry et al. 2019). Shallow troughs are the most common linear features present on the surface of the asteroid and a preliminary analysis agrees with the interpretation that Bennu is a rubble-pile asteroid that may contain large subsurface blocks or some other form of interior rigidity (Barnouin et al. 2019; Perry et al. 2019).

Besides decameter-long lineaments located on the surface of the NEAs, the formation and propagation of fractures is a common process seen on rocks and boulders (Delbo et al. 2014; Molaro et al. 2020a, 2020b). Cracking can be driven by different processes, such as stresses from impact and thermal cycling (Figures 10(C)–(E)), variation in tectonic stresses, volatile loss, and dehydration and can eventually lead to rock exfoliation, breakdown, and rockfalls. The morphology, arrangement, orientation, and spatial density of the fractures provide hints about the process(es) generating them. In the case of impact origin, fractures are expected to usually propagate along all azimuthal directions (although hoop stress can also be created circumferentially around an impact), while fractures presenting preferred direction orientation can be the result of cyclic Sun-induced thermal stresses, as in the case of rocks in Earth's midlatitude desert and on Mars (McFadden et al. 2005; Eppes et al. 2015). It has been shown that the temperature variations due to cycles between day and night can damage the material on airless bodies of our solar system, allowing the

nucleation and growth of microfractures due to the mechanical stresses induced by diurnal temperature cycles. Hence, thermal fatigue has been invoked for explaining the disintegration process of surface rocks and the production of regolith over spatial and temporal scales (Dombard et al. 2010; Delbo et al. 2014). In the case of Bennu, the evidence of fractured boulders (Figures 10(C) and (D)) coupled with the morphology of the rocks are consistent with models of fatigue-driven exfoliation (although impacts can also produce such morphologies) and demonstrate the possibility that crack propagation through thermal stress can lead to their development (Molaro et al. 2020b, 2020a). Better evidence for the effect of thermal fatigue is provided by an analysis of the orientation of boulder cracks on Ryugu, which reveal the existence of a preferred orientation in the meridional direction (Figure 10(E); Sasaki et al. 2021). On the other hand, on Itokawa, several cracked boulders have been observed and compared with cracked fragments generated by impact experiments, suggesting that impacts remain an important factor in generating rock cracks (Nakamura et al. 2008).

Expectations from DART and LICIACube. In the meter-scale DRACO images of Dimorphos, it may be possible to detect and analyze (if present) both global or local linear features located on the asteroid's surface. Recognition of longer lineaments on very rocky and rough surfaces could be complicated by the small handful of viewing geometries available. A nondetection may not mean that these features are not present. But if large and small lineaments are indeed seen, their presence will constrain the internal structure of Dimorphos when taking into account lessons from other NEAs. Such analyses will allow testing of Didymos and Dimorphos formation and evolution and provide insights into the stresses affecting the binary system. From the centimeter-scale DRACO images of the final DART impact site, it will be possible to detect the presence (if any) of cracks on Dimorphos boulders, therefore advancing the knowledge of fractures' formation processes, such as thermal fatigue, in the context of an S-type body.

4.3.5. Natural Particle Ejection

Active asteroids, small bodies that display activity but are not necessarily volatile rich or possess cometary origins (Nuth et al. 2020), exhibit mass ejection from mechanisms due to rotational instabilities and impacts and other nongravitational effects (Jewitt 2012; Jewitt et al. 2015). Among such activities, rotational-driven activities depend strongly on the geological (presence of loose unconsolidated rubble) surface and geophysical (spin-state) conditions (Hirabayashi et al. 2014; Nakano & Hirabayashi 2020; Barnouin et al. 2022; Jackson et al. 2022). Data collected at asteroid Bennu (Lauretta et al. 2019b; Chesley et al. 2020; Pelgrift et al. 2020; Hergenrother et al. 2020) highlight that natural particle ejection on asteroids (Jewitt 2012; Jewitt et al. 2015) is an important process and is probably an indicator of the geologic and geophysical state of small planetary bodies. The recent proximity observations of asteroid Bennu have suggested that besides rotational causes for particle ejections, additional mechanisms might be operating. An important contender remains mass ejection from micrometeoroid impacts (Bottke et al. 2020), and thermal fatigue (Molaro et al. 2020b; Rozitis et al. 2020). The presence of volatiles could also be a factor (Lauretta et al. 2019b). The ejected particle trajectories strongly depend on the complex force field surrounding Bennu, giving a relatively short particle lifetime (McMahon et al. 2020; Bierhaus et al. 2021), while the particles' influence on Bennu's dynamics is minimal (Scheeres et al. 2020). In addition, some ejecta particles escaping from Bennu finally may reach Earth (Kováčová et al. 2020).

There is a possibility that natural particle ejections may also occur in the Didymos system. Unlike the small bodies explored by spacecraft missions in the past, Didymos is a binary asteroid, which for most origin scenarios implies that particle ejection and the resulting dynamic behavior directly contributed to its formation and evolution. There are multiple processes generating mass ejection such as rotational instability, impacts, and nongravitation processes. Rotational instability may be one of the key processes causing mass ejection from Didymos because of its 2.26 hr spin period (Hirabayashi et al. 2017; Zhang et al. 2017, 2021; Naidu et al. 2020). A high centrifugal acceleration causes steep surface slopes (Zhang et al. 2017), possibly giving the entire body some sensitivity to structural failure (Naidu et al. 2020). Under this condition, failed regions may induce mass movements followed by particle ejection. Impacts and other nongravitational effects also play significant roles in particle ejection. Meteoroid impacts can expel grains with a wide range of ejection speeds (Gault et al. 1968; Richardson et al. 2007; Raducan et al. 2020, 2022). Large impacts can induce this process on a large scale (Stickle et al. 2022). Micrometeoroid impacts (Ballouz et al. 2020) may have limited influence on particle ejection but pulverize surface materials (Cambioni et al. 2021). The combination of this process with other nongravitational effects such as electrostatic lofting (Hartzell 2019), solar radiation pressure (McMahon et al. 2020), and thermal fracturing (Molaro et al. 2020b; Rozitis et al. 2020) can also lead to mass ejection.

Expectations from DART and LICIACube. Whether or not DART will be able to detect ejected particles remains a question. Interestingly, the system's L4 and L5 Lagrange points are linearly stable, meaning that these regions satisfy a condition that a small number of small particles can stay there. Though this does not mean that ejecta particles should exist there, these locations may scientifically be interesting to observe. However, DART's approach to observing particle ejection in the Didymos system is analogous to EPOXI's, which conducted observations of large particles in the coma of the hyperactive comet 103P/Hartley 2 during a flyby (Hermalyn et al. 2013). OSIRIS-REx used repeated long-duration observations to identify ejecta particles and track their trajectories to understand their origin and ultimate fate. Hayabusa and Hayabusa2 hovered over their respective target asteroids at near-uniform lighting conditions and never detected ejected particles, possibly because of unsuitable viewing geometries. Like EPOXI, the DART approach and the LICIACube flyby will have a short window of a few minutes to track particles around Didymos before these measurements are confounded by ejecta from the DART impact. With this type of data set, the particles' positions may be determined if observed for long enough by LICIACube to obtain stereo parallax, but measuring their velocities will be limited to those particles that exhibit detectable motions during the short window of observations. Thus, it may not be possible to characterize their trajectories in detail even if detected.

5. Observing the DART Crater: The DRACO Pre- and LEIA Post-impact Contextualization

As mentioned in Section 2.2, LICIACube will have its closest approach to Dimorphos ∼165 s after DART's kinetic

impact (Dotto et al. 2021) from a safe distance of 51 km. The size of the DART crater could range in diameter from 8 m (for a very strong target) to 100 m (for a zero-strength target; Stickle et al. 2022). Using crater-scaling rules (Housen et al. 1983: Housen & Holsapple 2011) the resulting crater formation times will then range from less than 1 s to a few tens of minutes. The timing of the close approach flyby would allow LICIACube to be able to observe some if not all of the DART crater formation process, but the ejecta plume may obscure LICIACube's view of Dimorphos' surface. The rate of the observed evolution will depend mostly on the strength (or lack thereof) and porosity of the target (Fahnestock et al. 2022). If the target tends stronger and crater formation is complete before closest approach (where the curtain is seen to separate from the crater rim), it will be possible to determine some of the surface geological properties from the crater diameter and possibly its depth. If the target tends weaker, then initial assessments of the excavated regions with the crater may be possible, if ejecta does not prevent the surface from being imaged by LICIACube. This assessment could include an exploration of non-space-weathered fresh interior material and possible uncovering of any near-surface layering via color variegation.

The DART spacecraft will target an impact location near the center of brightness of Dimorphos as revealed in the DRACO images (Rivkin et al. 2021). If the impact occurs near that center, then that location is generally expected to be near Dimorphos' equator at $-10°$ N, at a longitude of about 260° E. Once LICIACube passes CA, the crater will probably no longer be visible. As a result, if the target is truly weak, the future Hera mission will be the first to explore the final crater in 2027. Nevertheless, regardless of the target strength, the images of the DART ejecta may provide evidence for secondary boulders, and an ejecta pattern that could indicate how the terrain observed in the DRACO images is influencing the ejecta. In fact, the DART impact may well produce large quantities of ejected debris, some of which will fall back down onto the surface of Dimorphos or Didymos at low speed (Perry et al. 2022; Rossi et al. 2022; Raducan & Jutzi 2022). Analyzing the penetration depth of reaccreting or falling boulders using Hera images and reformulated granular dynamics (and soil mechanics) equations including a Froude number to account for the very low gravity (Sunday et al. 2022) will provide new constraints on the mechanical properties of the asteroid surface material to further elucidate the type of terrain encountered by DART.

The tools we plan to employ to assess the geology of both Dimorphos and Didymos, combined with past geological assessments of NEAs and our current understanding of the dynamics of binaries, provide us with the means to understand the local target conditions encountered by DART. This will also provide a way to infer some of the internal characteristics of Dimorphos, hence returning the most detailed pre-Hera characterization of the target.

6. Conclusion

The DART and LICIACube missions provide a wealth of information that can help to solve the origin and evolution conundrum of the Didymos system, as well as return important physical and chemical constraints on the near-surface and interior state of Dimorphos. These latter constraints will be important for understanding the consequences of the DART impact, including establishing some connection between the expected momentum transfer driven by a kinetic impactor and the observed geological and geophysical nature of an asteroid. This connection will be key for developing future missions that may actually need to divert an asteroid to protect Earth (Statler et al. 2022).

We also anticipate that the data collected by these two spacecraft will lead to new unexpected discoveries. Indeed, we have never visited a binary system, and the occurrence of mutual gravitational dynamics in such a system likely leads to consequences in observed geology we can only allude to, like the expected transport of particles between Didymos and Dimorphos, but which we do not truly understand. Therefore, thanks to the DRACO, LEIA, and LUKE images, we are likely to find new unanticipated geological features. We anticipate our observations will lead to new discoveries and new questions that will remain unanswered. But unlike most other targets of nonrendezvous small-body missions, there will be a very detailed post-impact geology assessment of Dimorphos and Didymos. Indeed, the ESA/Hera spacecraft and its cubesats will perform in early 2027 a global mapping with a spatial scale of $\sim$1 m pixel^{-1} at several spectral wavelengths (Michel et al. 2022). Large parts of the surface of Dimorphos (and possibly Didymos) will be imaged at a resolution of 40 cm during close observations, and the highest resolution may even be 10 cm locally. These data sets will permit comparisons of the pre-impact geology provided by DART/LICIACube and the post-impact one by Hera. We expect to determine how the DART impact transformed geologically the surface of Dimorphos and provide additional answers to all the new questions we will have on the origin and evolution of the Didymos system.

This work is dedicated to the memory of Prof. Stefano Debei, our friend and colleague who sadly left us ahead of time. The authors are grateful to the two anonymous reviewers for constructive and important comments, suggestions, and corrections that led to a substantial improvement of the paper. This work was supported by the Italian Space Agency (ASI) within the LICIACube project (ASI-INAF agreement AC n. 2019-31-HH.0). This work was supported by the DART mission, NASA Contract No. 80MSFC20D0004. E.A. is funded by the University of Arizona. S.S. acknowledges support from NASA as part of the Double Asteroid Redirection Test (DART) Participating Scientist Program. J.M.T.-R. is funded by the research project (PGC2018-097374-B-I00), funded by FEDER/Ministerio de Ciencia e Innovación—Agencia Estatal de Investigación. P.M. acknowledges ESA as well as funding from the French space agency CNES, from the European Union's Horizon 2020 research and innovation program under grant agreement No. 870377 (project NEO-MAPP) and from the CNRS through the MITI interdisciplinary programs.

Appendix

This appendix provides additional context that can be found elsewhere but may be helpful as an additional resource when considering the DART impact and the geology of Didymos and Dimorphos.

A.1. The NASA/Deep Impact Mission, Implications for Planetary Defense

The first planetary-scale impact experiment on a small body was conducted by the NASA/Deep Impact mission to comet 9P/Tempel 1, which delivered 19 GJ of kinetic energy via a 370 kg, ∼50% copper mass at 10.3 km s^{-1} (A'Hearn et al. 2005). While Deep Impact was focused on the science of revealing the interior composition and structure of the comet, its implications for planetary defense were recognized from the outset (A'Hearn & Johnson 2015). Among the key results from analyses of Deep Impact (A'Hearn et al. 2005; Schultz et al. 2007) and the flyby of Stardust NExT 5.5 yr later (Schultz et al. 2013; Veverka et al. 2013) relevant to DART's redirection test and LICIACube's observations are the effects controlled by the physical and geological properties of the target. These included a ∼30° oblique impact, weak particles with very high porosity, variations in near-surface composition, bright and long-lasting ejecta, infilling of the crater from high-angle ejecta fallback (due to porosity), and that impacts in small bodies hit surfaces that possess low strengths (<kPa; Richardson et al. 2007), but could also be gravity controlled (Schultz et al. 2007). Hayabusa2's Small Carry-on Impactor experiment into Ryugu confirmed some similar target effects on impacts on an NEA's surface (Arakawa et al. 2020).

A.2. NEAs Main Discoveries

A.2.1. The Silicate-rich NEAs

Among all visited NEAs, the largest one, called Eros ($34 \times 11 \times 11$ km size), is a low macroporous (∼20%; Wilkinson et al. 2002), cratered world, covered in unconsolidated surface regolith. The asteroid possesses several grooves and ridges (Veverka et al. 2000) that indicate the presence of broad planes of weakness that could have been produced by multiple impacts that shattered the asteroid and/or its parent body (e.g., Buczkowski et al. 2008; Tonge et al. 2016); alternatively, these structures may be fissures in fine-grained granular material (Asphaug et al. 2002). In either case, the extent of the lineaments provides some evidence for coherence across the asteroid (Marchi et al. 2015). Moreover, large boulders (>30 m in diameter) have been linked with the formation of the large 8 km size Shoemaker crater (IAU Charlois Regio) on the asteroid (Thomas et al. 2001), while a scarcity of small craters (0.177 to 1 km in diameter) near Shoemaker provides evidence for seismic shaking (Thomas & Robinson 2005). Some of the large boulders on Eros (which equal the size of Dimorphos) show aprons at their base, evidence of their slow breakdown.

Itokawa was the first unquestionable rubble-pile asteroid (Fujiwara et al. 2006) ever visited, with a low bulk density, high (∼40%) porosity, and boulder-rich appearance (Abe et al. 2006) as well as its elongated shape ($0.5 \times 2.9 \times 2.1$ km). In particular, its geology is dominated by two regions: a smooth low-lying region and a rougher boulder-rich highland (Fujiwara et al. 2006; Barnouin-Jha et al. 2008). Moreover, Itokawa looks to be composed of two parts that might have experienced collisional disruption followed by reaccumulation (Nakamura et al. 2008; Michel & Richardson 2013; Mazrouei et al. 2014).

Also elongated ($4.8 \times 2.4 \times 2.0$ km), Toutatis has a large crater at its observed limb, and like Itokawa, is characterized by a clear bilobate shape suggesting a contact binary origin. This asteroid possesses widespread evidence for boulders and regolith on its surface (Huang et al. 2013), and their identification has been possible despite a much coarser imagery data set than the other NEAs visited.

A.3. The Carbonaceous NEAs

Asteroids (162173) Ryugu ($1.04 \times 1.02 \times 0.88$ km) and (101955) Bennu ($0.57 \times 0.54 \times 0.51$ km) differ from these latter bilobate asteroids because they are top-shaped carbonaceous NEAs. Their low density and boulder-rich appearance confirm they are rubble piles (Barnouin et al. 2019; Watanabe et al. 2019) made from reaccumulated fragments of larger parent bodies that were catastrophically disrupted (Lauretta et al. 2019a; Sugita et al. 2019; Michel et al. 2020; Tatsumi et al. 2021). The top-shape structure is thought to be the result of rotational acceleration (spin-up) due to thermally driven torques (Walsh 2018; Hirabayashi & Scheeres 2019; Roberts et al. 2021) known as YORP (Rubincam 2000) or a consequence of the asteroid reaccumulation process (Michel et al. 2020). Both asteroids are covered with boulders—Ryugu possessing a slightly larger number density (Michikami et al. 2019) than Bennu (Burke et al. 2021)—but do not possess large regions of fine regolith similar to those observed on Itokawa. The largest (>20 m) of boulders on Bennu seem to retain smaller rocks and boulders and may contribute to the observed hemispherical shape differences (Daly et al. 2020a). Both asteroids possess evidence for some surface lineations whose origins are not well established (Barnouin et al. 2019; Sugita et al. 2019) and evidence for craters (Walsh et al. 2019; Hirata et al. 2020), with up to 1500 craters identified on the surface of Bennu (Bierhaus et al. 2022). The presence of mass movements and evidence for crater ejecta and terraces on Bennu indicate the near surface (top 10 m or so) may be very weak with cohesion below 100 Pa, and most likely <0.6 Pa (Barnouin et al. 2022; Perry et al. 2022), which is supported by analysis of spacecraft telemetry during the sampling event (Walsh et al. 2022) and the postsampling observations of the spacecraft-generated crater (Lauretta et al. 2022). The small carry-on impactor experiment (SCI) created an artificial crater on the surface of Ryugu and revealed a similarly low-strength regolith (Arakawa et al. 2020). These results for the near-surface strength of Bennu's and Ryugu's regolith stand in contrast to estimates of the tensile and compressive strengths of their meter-scale boulders, which are estimated to be on the order of 0.1 MPa and 1 MPa, respectively, as revealed by thermal measurements (Grott et al. 2019; Rozitis et al. 2020) and analysis of craters on boulders (Ballouz et al. 2020). These findings for boulder strength are consistent with values from the study of the tensile strength inferred from the typical heights and velocities measured for fragile chondrite meteoroids disintegrating in the atmosphere (Trigo-Rodríguez & Llorca 2006, 2007; Trigo-Rodríguez & Blum 2009). They are also consistent with size-dependent strength when measured tensile strengths of primitive meteorites are extrapolated to meter sizes (Cotto-Figueroa et al. 2016).

ORCID iDs

M. Pajola https://orcid.org/0000-0002-3144-1277
O. S. Barnouin https://orcid.org/0000-0002-3578-7750
A. Lucchetti https://orcid.org/0000-0001-7413-3058
M. Hirabayashi https://orcid.org/0000-0002-1821-5689

R.-L. Ballouz https://orcid.org/0000-0002-1772-1934
E. Asphaug https://orcid.org/0000-0003-1002-2038
C. M. Ernst https://orcid.org/0000-0002-9434-7886
V. Della Corte https://orcid.org/0000-0001-6461-5803
T. Farnham https://orcid.org/0000-0002-4767-9861
G. Poggiali https://orcid.org/0000-0002-3239-1697
J. M. Sunshine https://orcid.org/0000-0002-9413-8785
E. Mazzotta Epifani https://orcid.org/0000-0003-1412-0946
N. Murdoch https://orcid.org/0000-0002-9701-4075
S. Ieva https://orcid.org/0000-0001-8694-9038
S. R. Schwartz https://orcid.org/0000-0001-5475-9379
S. Ivanovski https://orcid.org/0000-0002-8068-7695
J. M. Trigo-Rodriguez https://orcid.org/0000-0001-8417-702X
A. Rossi https://orcid.org/0000-0001-9311-2869
N. L. Chabot https://orcid.org/0000-0001-8628-3176
A. Zinzi https://orcid.org/0000-0001-5263-5348
A. Rivkin https://orcid.org/0000-0002-9939-9976
J. R. Brucato https://orcid.org/0000-0002-4738-5521
P. Michel https://orcid.org/0000-0002-0884-1993
G. Cremonese https://orcid.org/0000-0001-9021-1140
E. Dotto https://orcid.org/0000-0002-9335-1656
M. Amoroso https://orcid.org/0000-0003-2603-165X
I. Bertini https://orcid.org/0000-0002-0616-2444
A. Capannolo https://orcid.org/0000-0002-4917-287X
B. Cotugno https://orcid.org/0000-0003-3868-8819
M. Dall'Ora https://orcid.org/0000-0001-8209-0449
R. T. Daly https://orcid.org/0000-0002-1320-2985
J. D. P. Deshapriya https://orcid.org/0000-0002-5758-1286
I. Gai https://orcid.org/0000-0002-5367-3650
P. H. A. Hasselmann https://orcid.org/0000-0003-1193-8945
G. Impresario https://orcid.org/0000-0001-8984-4231
M. Lavagna https://orcid.org/0000-0003-4361-1437
A. Meneghin https://orcid.org/0000-0003-1665-6664
D. Modenini https://orcid.org/0000-0002-1517-3938
P. Palumbo https://orcid.org/0000-0003-2323-9228
D. Perna https://orcid.org/0000-0002-4545-3850
S. Pirrotta https://orcid.org/0000-0003-0377-8937
E. Simioni https://orcid.org/0000-0001-5993-0868
S. Simonetti https://orcid.org/0000-0002-1309-2958
P. Tortora https://orcid.org/0000-0001-9259-7673
M. Zannoni https://orcid.org/0000-0002-4151-9656
G. Zanotti https://orcid.org/0000-0002-3157-7588

References

A'Hearn, M. F., & Johnson, L. N. 2015, in Handbook of Cosmic Hazards and Planetary Defense, ed. J. Pelton & F. Allahdadi (Cham: Springer), 513
Abe, M., Takagi, Y., Kitazato, K., et al. 2006, Sci, 312, 1334
Agrusa, H. F., Gkolias, I., Tsiganis, K., et al. 2021, Icar, 370, 114624
A'Hearn, M. F., Belton, M. J. S., Delamere, W. A., et al. 2005, Sci, 310, 258
Arakawa, M., Saiki, T., Wada, K., et al. 2020, Sci, 368, 67
Asphaug, E. 2008, M&PS, 43, 1075
Asphaug, E. 2009, AREPS, 37, 413
Asphaug, E., Eileen, V. R., & Zuber, M. T. 2002, in Asteroids III, ed. W. F. Bottke et al. (Tucson, AZ: Univ. Arizona Press), 463
Ballouz, R.-L., Walsh, K. J., Barnouin, O. S., et al. 2020, Natur, 587, 205
Barnouin, O. S., Daly, M. G., Palmer, E. E., et al. 2019, NatGe, 12, 247
Barnouin, O. S., Daly, M. G., Palmer, E. E., et al. 2020, P&SS, 180, 104764
Barnouin, O. S., Daly, M. G., Seabrook, J. A., et al. 2022, JGRE, 127, e06927
Barnouin, O. S., Noviello, J. L., & Ernst, C. M. 2014, LPSC, 45, 2221
Barnouin-Jha, O. S., Cheng, A. F., Mukai, T., et al. 2008, Icar, 198, 108
Bart, G. D. 2007, Icar, 187, 417
Bart, G. D., & Melosh, H. J. 2010, Icar, 209, 337
Beddingfield, C. B., Beyer, R. A., Singer, K. N., et al. 2020, Icar, 335, 113383
Benner, L. A. M., Busch, M. W., Giorgini, J. D., et al. 2015, in Asteroids IV, ed. P. Michel, F. E. DeMeo, & W. F. Bottke (Tucson, AZ: Univ. Arizona Press), 165
Benz, W., & Asphaug, E. 1999, Icar, 142, 5
Besse, S., Küppers, M., Barnouin, O. S., et al. 2014, P&SS, 101, 186
Bierhaus, E. B., Songer, J. T., Clark, B. C., et al. 2021, Icar, 355, 114142
Bierhaus, E. B., Trang, D., Daly, R. T., et al. 2022, NatGe, 15, 440
Bottke, W. F., Jr., & Melosh, H. J. 1996, Icar, 124, 372
Bottke, W. F., Jr., Moorhead, A. V., Connolly, H. C., Jr., et al. 2020, JGRE, 125, e06282
Brown, P., Spalding, R. E., ReVelle, D. O., et al. 2002, Natur, 420, 294
Buczkowski, D. L., Barnouin-Jha, O. S., & Prockter, L. M. 2008, Icar, 193, 39
Buczkowski, D. L., & Wyrick, D. Y. 2015, GSLSP, 401, 423
Burke, K. N., DellaGiustina, D. N., Bennett, C. A., et al. 2021, RemS, 13, 1315
Bus, S. J., & Binzel, R. P. 2002a, Icar, 158, 146
Bus, S. J., & Binzel, R. P. 2002b, Icar, 158, 106
Cambioni, S., Delbo, M., Poggiali, G., et al. 2021, Natur, 598, 49
Carr, M. H., Kirk, R. L., McEwen, A., et al. 1994, Icar, 107, 61
Cheng, A. F. 2002, in Asteroids III, ed. W. F. Bottke et al. (Tucson, AZ: Univ. Arizona Press), 351
Cheng, A. F., Barnouin, O. S., Hirata, N. H., et al. 2007, GeoRL, 34, L09201
Cheng, A. F., Michel, P., Jutzi, M., et al. 2016, P&SS, 121, 27
Cheng, A. F., Rivkin, A. S., Michel, P., et al. 2018, P&SS, 157, 104
Cheng, A. F., Weaver, H. A., Conard, S. J., et al. 2008, SSRv, 140, 189
Chesley, S. R., French, A. S., Davis, A. B., et al. 2020, JGRE, 125, e06363
Consolmagno, G. J., Britt, D. T., & Macke, R. J. 2008, ChEG, 68, 1
Cotto-Figueroa, D., Asphaug, E., Garvie, L. A. J., et al. 2016, Icar, 277, 73
Crosta, G. B., Frattini, P., Valbuzzi, E., et al. 2018, E&SS, 5, 89
Daly, M. G., Barnouin, O. S., Seabrook, J. A., et al. 2020a, SciA, 6, eabd3649
Daly, R. T., Barnouin, O. S., Bierhaus, E. B., et al. 2022a, Icar, 384, 115058
Daly, R. T., Bierhaus, E. B., Barnouin, O. S., et al. 2020b, GeoRL, 47, e89672
Daly, R. T., Ernst, C. M., Barnouin, O. S., et al. 2022b, PSJ, 3, 207
Delbo, M., Avdellidou, C., & Morbidelli, A. 2019, A&A, 624, A69
Delbo, M., Libourel, G., Wilkerson, J., et al. 2014, Natur, 508, 233
DellaGiustina, D. N., Burke, K. N., Walsh, K. J., et al. 2020, Sci, 370, eabc3660
DellaGiustina, D. N., Emery, J. P., Golish, D. R., et al. 2019, NatAs, 3, 341
DellaGiustina, D. N., Kaplan, H. H., Simon, A. A., et al. 2021, NatAs, 5, 31
Descamps, P., & Marchis, F. 2008, Icar, 193, 74
Dombard, A. J., Barnouin, O. S., Prockter, L. M., et al. 2010, Icar, 210, 713
Dotto, E., Della Corte, V., Amoroso, M., et al. 2021, P&SS, 199, 105185
Durda, D. D., Bottke, W. F., Jr., Enke, B. L., et al. 2004, Icar, 167, 382
Durda, D. D., Chapman, C. R., Cintala, M. J., et al. 2011, M&PS, 46, 149
Durda, D. D., Jedicke, R., & Greenberg, R. 1997, BAAS, 29, 974
El-Maarry, M. R., Thomas, N., Giacomini, L., et al. 2015, A&A, 583, A26
Eppes, M. C., Willis, A., Molaro, J., et al. 2015, NatCo, 6, 6712
Ernst, C. M., Barnouin, O. S., Daly, R. T., et al. 2018, LPSC, 49, 1043
Ernst, C. M., Barnouin, O. S., & Gaskell, R. W. 2012, LPSC, 43, 2393
Fahnestock, E. G., Cheng, A. F., Ivanovski, S., et al. 2022, PSJ, 3, 206
Fang, J., & Margot, J.-L. 2012a, AJ, 143, 24
Fang, J., & Margot, J.-L. 2012b, AJ, 143, 25
Fletcher, Z. J., Ryan, K. J., Maas, B. J., et al. 2018, Proc. SPIE, 10698, 106981X
Fujiwara, A., Kawaguchi, J., Teomans, D. K., et al. 2006, Sci, 312, 1330
Gaskell, R. W., Barnouin-Jha, O. S., Scheeres, D., et al. 2008, M&PS, 43, 1049
Gault, D. E., Quaide, W. L., & Oberbeck, V. R. 1968, in Shock Metamorphism of Natural Materials, ed. B. M. French & N. M. Short (Baltimore, MD: Mono Book), 87
Geissler, P., Petit, J. M., Durda, D. D., et al. 1996, Icar, 120, 140
Gehrels, T. 1994, Hazards Due to Comets and Asteroids (Tucson, AZ: Univ. Arizona Press)
Golombek, M. P., Huertas, A., Marlow, J., et al. 2008, JGRE, 113, E00A09
Grant, J. A., Wilson, S. A., Ruff, S. W., et al. 2006, GeoRL, 33, L16202
Grott, M., Knollenberg, J., Hamm, M., et al. 2019, NatAs, 3, 971
Guettler, C., Hirata, N., & Nakamura, A. M. 2012, Icar, 220, 1040
Harris, A. W., Fahnestock, E. G., & Pravec, P. 2009, Icar, 199, 310
Hartzell, C. M. 2019, Icar, 333, 234
Hergenrother, C. W., Maleszewski, C., Li, J.-Y., et al. 2020, JGRE, 125, e06381
Hermalyn, B., Farnham, T. L., Collins, S. M., et al. 2013, Icar, 222, 625
Hirabayashi, M., Scheeres, D. J., Sánchez, D. P., et al. 2014, ApJL, 789, L12
Hirabayashi, M., & Scheeres, D. J. 2019, Icar, 317, 354
Hirabayashi, M., Schwartz, S. R., Yu, Y., et al. 2017, MNRAS, 472, 1641
Hirata, N., Morota, T., Cho, Y., et al. 2020, Icar, 338, 113527
Honda, R., Arakawa, M., Shimaki, Y., et al. 2021, Icar, 366, 114530
Housen, K. R., & Holsapple, K. 2003, Icar, 163, 102

Housen, K. R., & Holsapple, K. A. 2011, Icar, 211, 856
Housen, K. R., Holsapple, K. A., & Voss, M. E. 1999, Natur, 402, 155
Housen, K. R., Schmidt, R. M., & Holsapple, K. A. 1983, JGR, 88, 2485
Huang, J., Ji, J., Ye, P., et al. 2013, NatSR, 3, 3411
Ieva, S., Mazzotta Epifani, E., Perna, D., et al. 2022, PSJ, 3, 183
Ivanov, B. 2006, in In Catastrophic Events Caused by Cosmic Objects, ed. V. Adushkin & I Nemchinov (Dordrecht: Springer), 91
Jackson, P. M., Nakano, R., Kim, Y., & Hirabayashi, M. 2022, PSJ, 3, 16
Jacobson, J. A., & Scheeres, D. J. 2011a, ApJL, 736, L19
Jacobson, S. A., Marzari, F., Rossi, A., et al. 2016, Icar, 277, 381
Jacobson, S. J., & Scheeres, D. J. 2011b, Icar, 214, 161
Jawin, E. R., McCoy, T. J., Walsh, K. J., et al. 2021, LPSC, 52, 2022
Jawin, E. R., McCoy, T. J., Walsh, K. J., et al. 2022, Icar, 381, 114992
Jawin, E. R., Walsh, K. J., Barnouin, O. S., et al. 2020, JGRE, 125, e06475
Jewitt, D. 2012, AJ, 143, 66
Jewitt, D., Hsieh, H., & Agrawal, J. 2015, in Asteroids IV, ed. P. Michel, F. E. DeMeo, & W. F. Bottke (Tucson, AZ: Univ. Arizona Press), 221
Kaplan, H. H., Lauretta, D. S., Simon, A. A., et al. 2020, Sci, 370, eabc3557
Kováčová, M., Nagy, R., Kornoš, L., et al. 2020, P&SS, 185, 104897
Kuiper, G. P. 1965, The Nature of the Lunar Surface (Baltimore, MD: The Johns Hopkins Press), 99
Küppers, M., Moissl, R., Vincent, J. B., et al. 2012, P&SS, 66, 71
Lambe, T. W., & Whitman, R. V. 1969, Soil Mechanics (New York: Wiley)
Lauretta, D. S., Adam, C. D., Allen, A. J., et al. 2022, Sci, 377, 285
Lauretta, D. S., DellaGiustina, D. N., Bennett, C. A., et al. 2019a, Natur, 568, 55
Lauretta, D. S., Hergenrother, C. W., Chesley, S. R., et al. 2019b, Sci, 366, eaay3544
Lee, P. C., Veverka, J., Thomas, P. C., et al. 1996, Icar, 120, 87
Lee, S. W., Thomas, P., & Veverka, J. 1986, Icar, 68, 77
Lucchetti, A., Penasa, L., Pajola, M., et al. 2019, GeoRL, 46, 14,336
Malin, M. C. 1992, JGR, 97, 16337
Malin, M. C., & Dzurisin, D. 1978, JGR, 83, 233
Marchi, S., Chapman, C. R., Barnouin, O. S., et al. 2015, in Asteroids IV, ed. P. Michel, F. E. DeMeo, & W. F. Bottke (Tucson, AZ: Univ. Arizona Press), 725
Margot, J.-L., Nolan, M. C., Benner, L. A. M., et al. 2002, Icar, 296, 1445
Margot, J.-L., Pravec, P., Taylor, P., et al. 2015, in Asteroids IV, ed. P. Michel, F. E. DeMeo, & W. F. Bottke (Tucson, AZ: Univ. Arizona Press), 355
Massironi, M., Marchi, S., Pajola, M., et al. 2012, P&SS, 66, 125
Mazrouei, S., Daly, M. G., & Barnouin, O. S. 2014, Icar, 229, 181
McCoy, T. J., Burbine, T. H., McFadden, L. A., et al. 2001, M&PS, 36, 1661
McFadden, L. D., Eppes, M. C., Gillespie, A. R., et al. 2005, GSAB, 117, 161
McMahon, J. W., Scheeres, D. J., Chesley, S. R., et al. 2020, JGRE, 125, e06229
Melosh, H. J. 1989, Impact Cratering: A Geologic Process, Oxford Monographs on Geology and Geophysics, 11 (Oxford Univ. Press, New York)
Melosh, H. J., & Ryan, E. V. 1997, Icar, 129, 562
Michel, P., Ballouz, R.-L., Barnouin, O., et al. 2020, NatCo, 11, 2655
Michel, P., Benz, W., Tanga, P., et al. 2001, Sci, 294, 1696
Michel, P., Cheng, A., Küppers, M., et al. 2016, AdSpR, 57, 2529
Michel, P., Küppers, M., Campo Bagatin, A., et al. 2022, PSJ, 3, 160
Michel, P., O'Brien, D. P., Abe, S., et al. 2009, Icar, 200, 503
Michel, P., & Richardson, D. C. 2013, A&A, 554, L1
Michikami, T., Honda, C., Miyamoto, H., et al. 2019, Icar, 331, 179
Michikami, T., Nakamura, A. M., Hirata, N., et al. 2008, EP&S, 60, 13
Miyamoto, H., Hemmi, R., Kikuchi, H., et al. 2019, LPSC, 50, 2398
Miyamoto, H., Yano, H., & Scheeres, D. J. 2007, Sci, 316, 1011
Molaro, J. L., Hergenrother, C. W., Chesley, S. R., et al. 2020a, JGRE, 125, e06325
Molaro, J. L., Walsh, K. J., Jawin, E. R., et al. 2020b, NatCo, 11, 2913
Moore, J. M., Asphaug, E., Morrison, D., et al. 1999, Icar, 140, 294
Murchie, S., Robinson, M., Clark, B., et al. 2002, Icar, 155, 145
Murdoch, N., Sánchez, P., Schwartz, S. R., et al. 2015, in Asteroids IV, ed. P. Michel, F. E. DeMeo, & W. F. Bottke (Tucson, AZ: Univ. Arizona Press), 767
Mutch, T. A., Arvidson, R. E., Bincer, A. B., et al. 1977, JGR, 82, 4452
Naidu, S. P., Benner, L. A. M., Brozovic, M., et al. 2020, Icar, 348, 113777
Nakamura, A. M. 2017, P&SS, 149, 5
Nakamura, A. M., Michikami, T., Hirata, N., et al. 2008, EP&S, 60, 7
Nakano, R., & Hirabayashi, M. 2020, ApJL, 892, L22
Noguchi, R., Hirata, N., Hirata, N., et al. 2021, Icar, 354, 114016
Nuth, J. A., III, Abreu, N., Ferguson, F. T., et al. 2020, PSJ, 1, 82
Pajola, M., Höfner, S., Vincent, J. B., et al. 2017b, NatAs, 1, 0092
Pajola, M., Lucchetti, A., Bertini, I., et al. 2016b, A&A, 585, A85
Pajola, M., Lucchetti, A., Fulle, M., et al. 2017a, MNRAS, 469, S636
Pajola, M., Lucchetti, A., Senter, L., et al. 2021, Univ, 7, 82
Pajola, M., Lucchetti, A., Vincent, J. B., et al. 2016a, A&A, 592, L2
Pajola, M., Mergili, M., Cambianica, P., et al. 2022, Icar, 375, 114850
Pajola, M., Rossato, S., Baratti, E., et al. 2017c, Icar, 296, 73
Pajola, M., Vincent, J. B., Güttler, C., et al. 2015, A&A, 583, A37
Palmer, E. E., Gaskell, R., Daly, M. G., et al. 2022, PSJ, 3, 102
Pelgrift, J. Y., Lessac-Chenen, E. J., Adam, C. D., et al. 2020, E&SS, 7, e2019EA000938
Perna, D., Barucci, M. A., & Fulchignoni, M. 2013, A&ARv, 21, 65
Perna, D., Fulchignoni, M., Barucci, M. A., et al. 2017, A&A, 600, A115
Perry, M., Barnouin, O., Daly, R. T., et al. 2022, NatGe, 15, 447
Perry, M. E., Barnouin, O. S., Jawin, E. R., et al. 2019, EPSC-DPS Joint Meeting 2019, EPSC–DPS2019–686
Pilorget, C., Okada, T., Bibring, J.-P., et al. 2022, NatAs, 6, 221
Poggiali, G., Brucato, J. R., Dotto, E., et al. 2021, Icar, 354, 114040
Poggiali, G., Brucato, J. R., Hasselmann, P. H., et al. 2022, PSJ, 3, 161
Pravec, P., & Harris, A. W. 2007, Icar, 190, 250
Pravec, P., & Scheirich, P. 2022, Icar, submitted
Pravec, P., Harris, A. W., Kušnirák, P., et al. 2012, Icar, 221, 365
Pravec, P., Scheirich, P., Kušnirák, P., et al. 2006, Icar, 181, 63
Pravec, P., Scheirich, P., Kušnirák, P., et al. 2016, Icar, 267, 267
Pravec, P., Thomas, C. A., Rivkin, A. S., et al. 2022, PSJ, 3, 175
Prockter, L., Thomas, P., Robinson, M., et al. 2002, Icar, 155, 75
Raducan, S. D., Davidson, T. M., & Collins, G. S. 2020, P&SS, 180, 104756
Raducan, S. D., Davidson, T. M., & Collins, G. S. 2022, Icar, 374, 114793
Raducan, S. D., & Jutzi, M. 2022, PSJ, 3, 128
Richardson, D. C., Agrusa, H. F., Barbee, B., et al. 2022, PSJ, 3, 157
Richardson, D. C., Elankumaran, P., Sanderson, R. E., et al. 2005, Icar, 173, 349
Richardson, D. C., & Walsh, K. J. 2006, AREPS, 34, 47
Richardson, J. E., Melosh, H. J., Lisse, C. M., et al. 2007, Icar, 191, 176
Rivkin, A. S., Chabot, N., Stickle, A. M., et al. 2021, PSJ, 2, 173
Rizk, B., Drouet d'Aubigny, C., Golish, D., et al. 2018, SSRv, 214, 26
Rizos, J., de Léon, J., Licandro, J., et al. 2021, Icar, 364, 114467
Roberts, J. H., Barnouin, O. S., Daly, M. G., et al. 2021, P&SS, 204, 105268
Robinson, M. S., Thomas, P. C., Veverka, J., et al. 2002, M&PS, 37, 1651
Rossi, A., Marzari, F., & Brucato, J. R. 2022, PSJ, 3, 118
Rozitis, B., Emery, J. P., Siegler, M. A., et al. 2020, JGRE, 125, e06323
Rubincam, D. P. 2000, Icar, 148, 2
Ryan, E. V., & Melosh, H. J. 1997, Icar, 133, 1
Sasaki, S., Saito, J., Ishiguro, M., et al. 2006, LPSC, 37, 1671
Sasaki, S., Honda, C., Sugita, S., et al. 2021, 43rd COSPAR Scientific Assembly, 270
Sasaki, S., Kanda, S., Kikuchi, H., et al. 2019, LPI Contribution, 2189, 2098
Scheeres, D. J. 2007, Icar, 189, 370
Scheeres, D. J., McMahon, J. W., Brack, D. N., et al. 2020, JGRE, 125, e06284
Schenk, P. M., & Bulmer, M. H. 1998, Sci, 279, 1514
Schmidt, B. E., Hughson, K. H. G., Chilton, H. T., et al. 2017, NatGe, 10, 338
Schröder, S. E., Carsenty, U., Hauber, E., et al. 2020, E&SS, 8, e00941
Schröder, S. E., Carsenty, U., Hauber, E., Raymond, C. A., & Russell, C. T. 2021, PSJ, 2, 111
Schultz, P. H., Eberhardy, C. A., Ernst, C. M., et al. 2007, Icar, 191, 84
Schultz, P. H., Hermalyn, B., & Veverka, J. 2013, Icar, 222, 502
Shi, X., Oberst, J., & Willner, K. 2016, GeoRL, 43, 12,371
Shoemaker, E. M., & Morris, E. C. 1970, Icar, 12, 188
Sierks, H., Barbieri, C., Lamy, P., et al. 2015, Sci, 347, aaa1044
Sierks, H., Lamy, P., Barbieri, C., et al. 2011, Sci, 334, 487
Simioni, E., Pajola, M., Massironi, M., et al. 2015, Icar, 256, 90
Singer, K. N., McKinnon, W. B., Schenk, P. M., et al. 2012, NatGe, 5, 574
Statler, T. S., Raducan, S. D., Barnouin, O. S., et al. 2022, PSJ, submitted
Stickle, A., Burger, C., Caldwell, W. K., et al. 2022, PSJ, submitted
Sugita, S., Honda, R., Morota, T., et al. 2019, Sci, 364, eaaw0422
Sullivan, R., Greeley, R., Pappalardo, R., et al. 1996, Icar, 120, 119
Sullivan, R. J., Thomas, P. C., Murchie, S. L., et al. 2002, in Asteroids III, ed. W. F. Bottke, Jr. et al. (Tucson, AZ: Univ. Arizona Press), 331
Sunday, C., Murdoch, N., Wilhelm, A., et al. 2022, A&A, 658, A118
Susorney, H. C. M., Johnson, C. L., Barnouin, O. S., et al. 2019, Icar, 325, 141
Susorney, H. C. M., Philpott, L. C., Ballouz, R. L., et al. 2021, Icar, 357, 114265
Tanbakouei, S., Trigo-Rodríguez, J. M., Sort, J., et al. 2019, A&A, 629, A119
Tardivel, S., Sánchez, P., & Scheeres, D. J. 2018, Icar, 304, 192
Tatsumi, E., Sugimoto, C., Riu, L., et al. 2021, NatAs, 5, 39
Tatsumi, E., & Sugita, S. 2018, Icar, 300, 227
Tholen, D. J. 1989, in Asteroids II, ed. T. Gehrels, R. P. Binzel, & M. S. Matthews (Tucson, AZ: Univ. Arizona Press), 1139

Tholen, D. J., & Barucci, M. A. 1989, in Asteroids II, ed. T. Gehrels, R. P. Binzel, & M. S. Matthews (Tucson, AZ: Univ. Arizona Press), 298
Thomas, N., Barbieri, C., Keller, H. U., et al. 2012, P&SS, 66, 96
Thomas, P. C., Joseph, J., Carcich, B., et al. 2002, Icar, 155, 18
Thomas, P. C., & Prockter, L. M. 2010, in Planetary Tectonics, ed. T. R. Watters & R. A. Schultz (New York: Cambridge Univ. Press), 233
Thomas, P. C., & Robinson, M. S. 2005, Natur, 436, 366
Thomas, P. C., Veverka, J., Robinson, M. S., et al. 2001, Natur, 413, 394
Tonge, A. L., Ramesh, K. T., & Barnouin, O. 2016, Icar, 266, 76
Trigo-Rodríguez, J. M., & Blum, J. 2009, P&SS, 57, 243
Trigo-Rodríguez, J. M., & Llorca, J. 2006, MNRAS, 372, 655
Trigo-Rodríguez, J. M., & Llorca, J. 2007, MNRAS, 375, 415
Tsuchiyama, A., Uesugi, M., Matsushima, T., et al. 2011, Sci, 333, 1125
Tsuchiyama, A., Uesugi, M., Uesugi, K., et al. 2014, M&PS, 49, 172
Veverka, J., Belton, M., Klaasen, K., et al. 1994, Icar, 107, 2
Veverka, J., Helfenstein, P., Lee, P., et al. 1996, Icar, 120, 66
Veverka, J., Klaasen, K., A'Hearn, M., et al. 2013, Icar, 222, 424
Veverka, J., Robinson, M., Thomas, P., et al. 2000, Sci, 289, 2088
Veverka, J., Thomas, P., Harch, A., et al. 1999, Icar, 140, 3
Veverka, J., Thomas, P. C., Robinson, M., et al. 2001, Sci, 292, 484
Walsh, K. J. 2018, ARA&A, 56, 593
Walsh, K. J., Ballouz, R.-L., Jawin, E. R., et al. 2022, SciA, 8, eabm6229
Walsh, K. J., & Jacobson, S. A. 2015, in Asteroids IV, ed. P. Michel, F. E. DeMeo, & W. F. Bottke (Tucson, AZ: Univ Arizona Press), 375
Walsh, K. J., Jawin, E. R., Ballouz, R.-L., et al. 2019, NatGe, 12, 242
Walsh, K. J., & Richardson, D. C. 2006, Icar, 180, 201
Walsh, K. J., Richardson, D. C., & Michel, P. 2008, Natur, 454, 188
Walsh, K. J., Richardson, D. C., & Michel, P. 2012, Icar, 220, 514
Watanabe, S., Hirabayashi, M., Hirata, N., et al. 2019, Sci, 364, 268
Wilkinson, S. L., Robinson, M. S., Thomas, P. C., et al. 2002, Icar, 155, 94
Xiao, Z., Zeng, Z., Ding, N., & Molaro, J. 2013, E&PSL, 376, 1
Yada, T., Abe, M., Okada, T., et al. 2022, NatAs, 6, 214
Yingst, R. A., Crumpler, L., Farrand, W. H., et al. 2010, JGRE, 115, E00F13
Yingst, R. A., Haldemann, A. F. C., Biedermann, K. L., et al. 2007, JGRE, 112, E06002
Zhang, Y., Michel, P., Richardson, D. C., et al. 2021, Icar, 362, 114433
Zhang, Y., Richardson, D. C., Barnouin, O. S., et al. 2017, Icar, 294, 98